



Hydro-mechanical and gas transport (HM-G) characterization of sand/bentonite mixture within the framework of the Gas Permeable Seal Test (GAST)

Erdem Toprak¹ · Sebastia Olivella^{1,2} · Enrique Romero^{1,2} · Alessandro Fraccica³ · George William Lanyon⁴

Received: 6 September 2025 / Accepted: 21 March 2026
© The Author(s) 2026

Abstract

The sand/bentonite (S/B) mixture is considered as a candidate sealing and backfilling material for Switzerland's deep geological repository (DGR). Using S/B mixtures as sealing material offers key advantages, such as higher intrinsic gas permeability and lower swelling pressure, which enhance gas transport efficiency. These properties make the S/B mixture a strong candidate for use as a gas-permeable seal within the Engineered Gas Transport System (EGTS) concept. This study investigates the coupled hydro-mechanical and gas transport (HM-G) response of the S/B mixture, incorporating the effects of dynamic compaction-induced variability in dry density. Key properties of the S/B mixture, such as porosity-dependent and strain-dependent water retention curves (WRC), effective and intrinsic water and gas permeability, and mechanical parameters, were calibrated while accounting for the process-driven heterogeneity in dry density and effective gas permeability of the system. Laboratory-scale simulations of oedometer and swelling pressure tests were conducted to support the parametrization of the mechanical model. The calibrated parameters were then implemented in a 3D small-scale model to evaluate the THM-G response of the S/B mixture, accounting for material heterogeneity under conditions representative of GAST, involving sequential hydration and gas injection stages. The simulations were performed using CODE_BRIGHT, a Finite Element Method (FEM) program. Advanced geo-mechanical models, including the Barcelona Basic Model (BBM), the Barcelona Expansive Model (BExM), and a strain-dependent intrinsic permeability formulation, were employed to represent the material behaviour within a continuum framework.

Keywords GAST · DGR design · EGTS · Sand/bentonite mixture · CODE_BRIGHT

Introduction

The understanding of gas migration and its potential impact on the engineered barrier system (EBS) and host rock has been a key focus for Nagra in Switzerland (Diomidis et al.

2016). The evolution of gas-related processes that could influence the long-term behavior and safety of repositories for low- and intermediate-level waste (L/ILW) and high-level waste (HLW) in Opalinus Clay is documented in Nagra (2008), Marschall et al. (2005) and Senger et al. (2018). Opalinus Clay has been selected as the preferred host rock for an L/ILW repository in Switzerland due to its low permeability, which makes it an effective barrier against radionuclide transport. However, gas migration within an L/ILW repository poses a critical challenge for safety assessments in such low-permeability formations.

As illustrated in Fig. 1 a gas-permeable backfill and tunnel seals facilitate controlled gas release into the operation and access tunnels. This approach avoids compromising the low hydraulic conductivity of the host rock through mitigation of excessive gas pressures and an uncontrolled transport of gas through the host rock. The design of the sealing and

✉ Erdem Toprak
erdem.toprak@upc.edu

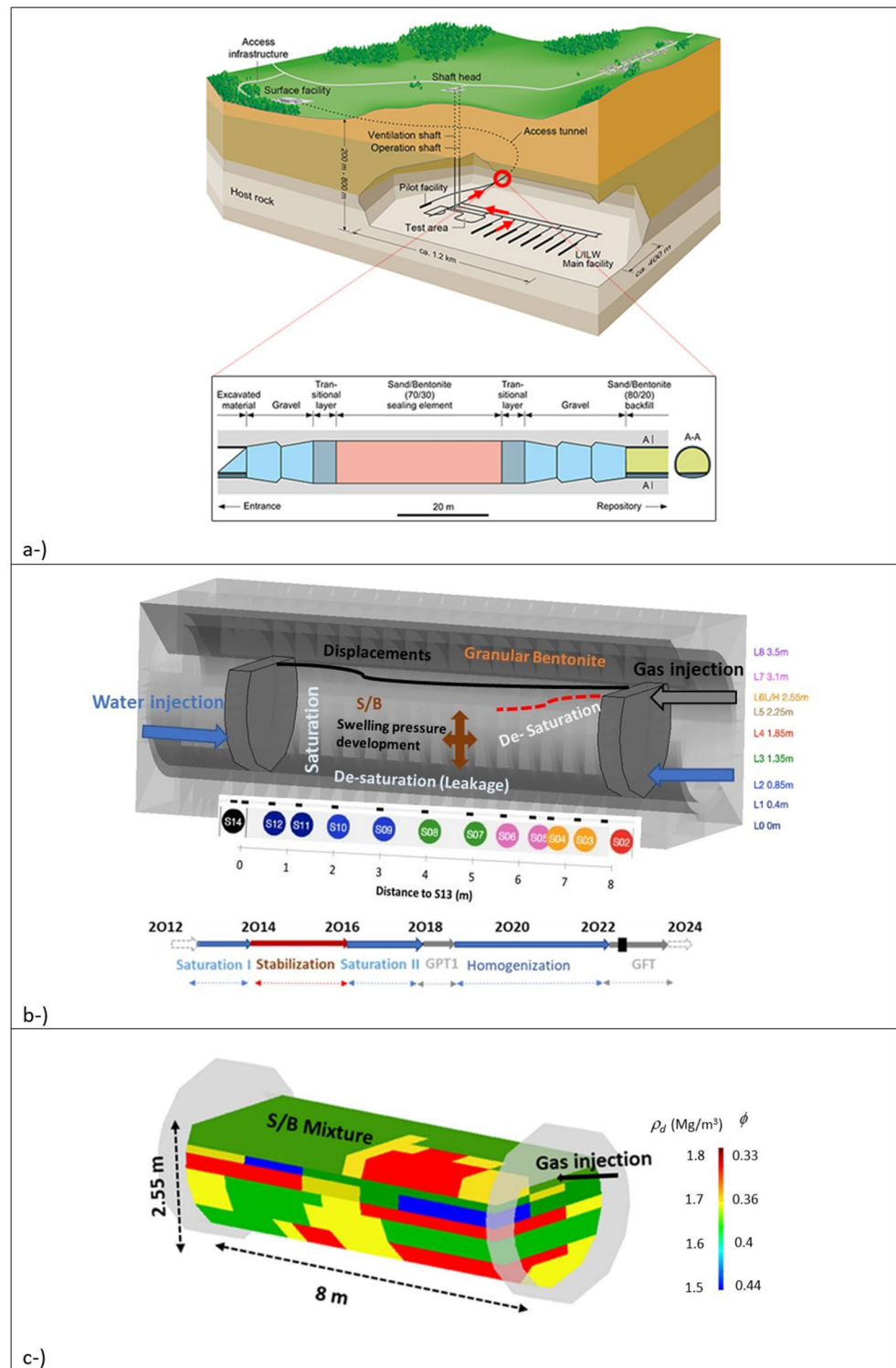
¹ International Centre for Numerical Methods in Engineering (CIMNE), Barcelona, Spain

² Department of Civil and Environmental Engineering, Universitat Politècnica de Catalunya, Barcelona, Spain

³ Department of the Geological Survey of Italy, Italian Institute for Environmental Protection and Research, ISPRA, Rome, Italy

⁴ Fracture Systems Ltd, St Ives, Cornwall, UK

Fig. 1 Conceptual design of gas pathways in the repository (a, Nagra (2008)). HM-G processes taking place in GAST (b); and initial dry density distribution within the S/B domain based on the data interpretation from Sakaki et al. (2023) (c)



backfill system is key to the fate of gases and repository performance with regard to gas-induced effects.

To investigate the gas transport mechanism in engineered-gas transport system and demonstrate sufficient gas transport capacity in realistic scale, the Gas Permeable Seal Test (GAST) was developed (Rüedi et al. 2012; Spillmann

et al. 2015) and conducted at the Grimsel Test Site (GTS) in Switzerland.

Figure 1b shows a schematic 3D representation of the GAST experiment layout. The configuration includes an 8-meter-long body of S/B mixture (80% sand and 20% bentonite) positioned between two gravel filters, which

facilitate water and gas injection or circulation. Additionally, the setup features granular bentonite (Seiphoori, 2015) at the interface between the S/B and the granitic host rock, and bentonite block walls sealing the filters against fluid loss. A retaining wall and concrete plug support the structure on the air-facing side of the gallery. For details on the construction, materials and instrumentation, readers are referred to Rüedi et al. (2012). The monitoring aspects can be found in Lanyon et al. (2022).

The S/B material, was emplaced and in situ compacted using dynamic compaction in 10 cm thick layers. Sampling during emplacement revealed a certain heterogeneity (Rüedi et al. 2012) in dry density that was induced by the compaction process. The heterogeneous configuration for the initial dry density distribution (Fig. 1c) in this study was generated based on the work of Sakaki et al. (2023).

Previous studies (Komine and Ogata 1999) showed that bentonite contents of 5–10% were insufficient to fill the voids between sand particles during wetting, whereas mixtures with 20% or more bentonite achieved complete void filling. The 20/80 sand–bentonite ratio thus provides effective sealing performance (Nagra 2008) while maintaining material efficiency (Sakaki et al. 2023) and optimising cost.

The GAST experiment commenced in July 2012 with hydration initiated from the sand filter closest to the concrete plug. The sequential water and gas injection through engineered barriers (S/B mixture and granular bentonite) gives rise to a series of processes that interact with each other in a complex way. In order to properly examine coupled effects (Fig. 1b), these individual processes must be simulated adequately by the numerical analysis.

During the experiment, the engineered barrier system was subjected to coupled thermo-hydro-mechanical–gas (THM-G) processes, while geochemical coupling was beyond the scope of this study. The sand–bentonite (S/B) mixture, granular bentonite (GB), and bentonite blocks were initially unsaturated and progressively saturated during the hydration stages (Saturation I, Saturation II, and Homogenisation). Hydration induced swelling pressures in the S/B mixture and GB, leading to stress redistribution and potential interface displacements. The development of swelling pressure during hydration and the reduction in mean total stress during gas injection due to de-saturation represent the principal HM-G coupling mechanisms considered. Temperature influences vapour diffusion through its role in the diffusion coefficient and psychrometric relationship; although temperature variations during the test were limited, minor local effects on suction and stress may occur.

Gas migration into clay barriers was investigated in various international projects, such as the FORGE project (2009–2013), DECOVALEX project (2019–2023) and finally EURAD-Gas project (2018–2024). In FORGE, gas

migration issues in repository performance assessment were investigated (Norris et al. 2015). In DECOVALEX-2019 (Tamayo-Mas et al. 2021), various types of modelling approaches were developed. One of the biggest challenges as explained by Tamayo-Mas et al. 2024 was to characterize and localize dilatancy-controlled flow in the models performed by several teams. EURAD-GAS (EURAD 2024) was built on the outcomes of FORGE; focused on the mechanistic understanding of gas transport in clay material. Development of gas pathways for clay-based materials has been investigated mainly at laboratory scale (Delahaye and Alonso 2002; Gerard et al. 2014; Gonzalez-Blanco and Romero 2022; Harrington et al. 2019; Jockwer and Wieczorek 2008; Wiseall et al. 2015; Gutiérrez-Rodrigo et al. 2015, 2021). There is also a variety in numerical approaches used to represent localised gas flow behaviour under saturated conditions, often incorporating arbitrary heterogeneity configurations and primarily relying on elastic formulations (Damians et al. 2020; Guo and Fall 2018; Radeisen et al. 2023; Noghretab et al. 2024 and, Toprak et al. 2025a).

To realistically model the THM-G processes occurring in the S/B mixture during the water and gas injection stages of the GAST experiment, validated material model parameters, i.e. parameters derived from simulations of laboratory-scale tests, are essential. This study establishes calibrated HM-G material model parameters for the S/B mixture, providing a foundation for future full-scale modelling calculations. Objectives, methodology, novelty and limitations of the study are briefly described below.

Objectives The primary objective of the GAST experiment is to demonstrate the effective functionality of gas-permeable seals composed of S/B mixtures under realistic scale and boundary conditions (Lanyon et al. 2022). The objective of the modelling work supporting GAST is to establish a representative numerical framework for subsequent full-scale simulations, comprising: (i) parameterisation of the hydro-mechanical and gas transport material models implemented in the numerical code, based on laboratory-scale mechanical and hydraulic tests (oedometer, infiltration, WRC, and permeability tests); and (ii) development of a representative 3D model configuration, including geometry and process-driven heterogeneity in initial dry density and effective gas permeability.

Methodology The methodology protocol foresaw five major modelling steps. The first step (1) involved developing a 3D GAST configuration that incorporates spatial variations in initial dry density (Fig. 1c), arising from dynamic compaction during the emplacement of the S/B mixture, as discussed by Sakaki et al. (2023). Secondly, based on the

dry density variation, porosity dependent WRC, water (Sect. [Hydraulic Process](#)) and gas permeabilities (Sect. [Gas Flow Mechanism and Gas Transport Model Parameters](#)) have been calibrated (2) by means of using test data of Manca (2015) and Manca et al. 2016. Once porosity and/or strain dependent hydro-gas model parameters were determined, oedometer tests (Romero et al. 2023) were simulated (3) for different values of dry densities. A swelling pressure test (Sect. [Mechanical Model Parameters](#)) was designed and simulated (4) under different mechanical models such as the Barcelona Basic Model (BBM, Alonso et al. 1990) and the Barcelona Expansive Model (BexM, Gens and Alonso 1992), to evaluate their respective capabilities and limitations. These models are considered alternative approaches for simulating HM-G response of S/B mixture within full-scale modelling of GAST.

In the final phase, a representative heterogeneous configuration of the GAST experiment (as described in Sect. [Impact of Heterogeneity in a Representative Model Configuration for GAST](#)) was proposed, incorporating potential zones of varying gas permeabilities (5). These zones can be identified through back-calculation of piezometer and pressure data once the test results become publicly available.

The modelling strategy is based on a ‘3D full modelling’ approach, comprising three key elements: (i) fully coupled processes, recognizing that hydro-mechanical interactions significantly affect gas transport within clay rich materials (EURAD 2024); (ii) representation of the full 3D geometry, acknowledging that heterogeneity in both dry density and effective gas permeability and (iii) inclusion of all test stages within the model, as the outcomes of earlier stages have a substantial impact on subsequent ones.

This study presents a potential configuration for 3D full modelling of localized gas flow in GAST, accounting for process-driven heterogeneity including spatial variations in dry density and effective gas permeability. Additionally, this study provides a novel application of an extended version of the Barcelona Basic Model (BBM) that incorporates dry density dependency of swelling pressure (Sect. [Mechanical Model Parameters](#)).

Hydro-mechanical and Gas Transport (HM-G) material model calibration

In CODE_BRIGHT (Olivella et al. 2023) there are several model options for WRC, intrinsic and effective water and gas permeability and mechanical models. CODE_BRIGHT has previously been employed in both construction (Toprak et al. 2017, 2020) and operation (Toprak et al. 2024, 2025b) licensing applications for final deep geological repositories

(DGRs) in various countries. The present study employed porosity- and strain-dependent hydro-gas models to provide a physically representative description of gas transport behaviour in the S/B mixture within the adopted continuum framework. This was achieved through the processing of experimental data from Manca (2015) and numerical simulation of oedometer tests conducted by Romero et al. (2023).

Hydraulic process

Porosity dependent WRC (Eq. (1) to (3)) is a well-recognized phenomenon in DGR design (Villar et al. 2007). The porosity dependent WRC on which the approach in the following is based on is the van Genuchten equation (van Genuchten 1980).

The water retention curve is defined as:

$$S_l(p_l) = \left(1 + \left(\frac{P_g - P_l}{P} \right)^{\frac{1}{1-y}} \right)^{-y} \tag{1}$$

With $P = P_0 \frac{\sigma}{\sigma_0}$, where P_0 is the air entry value at a certain temperature, σ_0 the water surface.

tension at that temperature and σ the surface tension as function of the temperature. S_l is liquid saturation, P_g is gas pressure and P_l is liquid pressure.

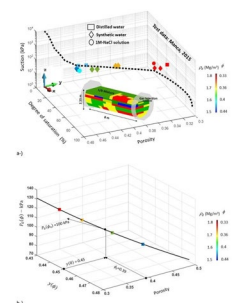
The parameters P (reference pressure) and y (shape function) are determined for different porosities (ϕ) following the relations, where ϕ_0 denotes the reference porosity, and “ C ” and “ D ” are model-specific calibration parameters:

$$P_0(\phi) = P_0 \exp(C(\phi_0 - \phi)) \tag{2}$$

$$y(\phi) = y \exp(D(\phi_0 - \phi)) \tag{3}$$

The porosity (ϕ) - degree of saturation (S_l) -suction (s) path is depicted as a continuous function for the S/B mixture material in Fig. 2a. Under the same suction value, different degree of saturations have been succeeded for different level of porosities following Eq. (2) and Eq. (3). The characteristic of the tested specimens (type of water, initial dry density,

Fig. 2 Water retention curve for different porosities (a) and evolution of reference pressure $P_0(\phi)$ and shape function $y(\phi)$ according to porosity (b)



porosity, suction and degree of saturation) was taken from Manca (2015). The test data was classified according to porosity and type of water. The colours correspond to porosity levels and the shapes (rectangle, diamond and circle) correspond to type of water. The target dry densities were 1.5 Mg/m³, 1.65 Mg/m³ and 1.8 Mg/m³, respectively. Distilled water (DW), synthetic water (SW) and 1 M-NaCl solution were used in the test. Following the dry density distribution of GAST, four levels of porosities (0.33, 0.36, 0.4 and 0.44) have been considered in order to represent the porosity dependent WRC models.

The air entry value, defined as the value of matric suction above which the gas starts to invade the larger pores of the soil, is usually higher for specimens compacted to lower porosity (Fig. 2b).

Porosity dependent WRC parameters are presented in Table 1. The reference porosity ϕ_0 was set to 0.39 for the calibration of WRC curve as listed in Table 1 and illustrated in Fig. 2b.

This porosity-dependent WRC can be applied within the framework of classical two-phase flow, where gas entry displaces pore water from the voids, governing the gas-water interaction in the porous medium. To calibrate the permeability model parameters (intrinsic and relative), test data derived from Manca (2015) and Romero et al. (2023) were utilized. The intrinsic permeability k (m²) for the related phase a (liquid: water or gas) is calculated as below (Eq. (4)), where K (m/s) is the hydraulic conductivity

of Darcy, μ (Pa.s) is the dynamic viscosity, ρ (kg/m³) is the density of the corresponding phase and g (m/s²) is the gravitational constant.

$$k_a = -K_a \frac{\mu_a}{\rho_a g} \tag{4}$$

The porosity-dependent permeability model (Eq. (5) to (7)) considers a continuum medium and Kozenys model (details in **CODE_BRIGHT**) which is defined as shown below, where k_0 is the reference intrinsic permeability (m²) and ϕ_0 is the reference porosity.

$$k_{Kozeny} = k_0 \frac{\phi^3}{(1 - \phi)^2} \frac{(1 - \phi_0)^2}{\phi_0^3} \tag{5}$$

The relative water permeability depends on the degree of saturation (here k_{rl} is relative water permeability and saturation is S_l) and the parameters A and Ω .

$$k_{rl} = A_l S_l^{\Omega_l} \tag{6}$$

Finally, the effective water permeability k_{effI} (m²) is defined as a product of the porosity-dependent permeability (k_{Kozeny}) and the relative water permeability (k_{rl}).

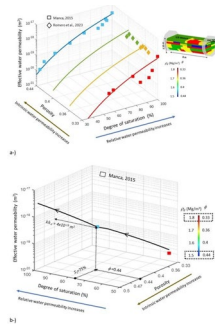
$$k_{effI} = k_{Kozeny} k_{rl} \tag{7}$$

Table 1 Hydro-gas model parameters for S/B mixture

Equation	Parameter	Units	Symbol	k_{Cubic1}	k_{Cubic2}	Data source
van Genuchten retention curve	Capillary pressure parameter (in $P(\phi)$)	(MPa)	P_0	0.1	0.1	Manca (2015)
Porosity-dependent WRC	Parameter for porosity influence (in $P(\phi)$)	(-)	C	3	3	
	Shape parameter in $y(\phi)$	(-)	y_0	0.45	0.45	
	Parameter for porosity influence (in $y(\phi)$)	(-)	D	-0.5	-0.5	
Advective Darcy flux Porosity-dependent permeability	Reference intrinsic permeability ($k_x = k_y$)	(m ²)	k_0	5×10^{-17}	5×10^{-17}	Manca (2015)
	Reference intrinsic permeability (k_z)	(m ²)	k_0	5×10^{-18}	5×10^{-18}	Sakaki et al. (2023)
	Reference porosity	(-)	ϕ_0	0.39	0.39	Romero et al. (2023)
Relative water permeability	Relative water permeability – constant	(-)	A	1	1	Romero et al. (2023)
	Relative water permeability – power	(-)	Ω	3	3	
Relative gas permeability	Relative gas permeability – constant	(-)	A	100*	100	
	Relative gas permeability – power	(-)	Ω	2	2	
Strain-dependent permeability (cubic law)	Initial aperture to calculate a variable aperture	(m)	b_0	3e-7	2e-6	Manca (2015)
	Spacing of the apertures:	(m)	a	1e-5	1e-3	
	Reference strain to calculate aperture variations	(-)	ϵ_0	1e-3	1e-3	
	Maximum aperture. Upper bound of aperture.	(m)	b_{max}	5e-6	5e-6	

*For the matrix A = 20

Fig. 3 Porosity – degree of saturation – effective water permeability (k_{effI}) path for four different initial dry densities (a) and a continuous calibration line of porosity- degree of saturation- effective water permeability path (b)



As shown in Fig. 3a, on one hand k_{effI} depends on porosity and on the other hand it depends on degree of saturation. In general, a larger porosity corresponds to a higher intrinsic water permeability. As observed in the laboratory tests, the S/B mixture with initially lower porosity exhibits lower effective water permeability for the same saturation level. Conversely, as the dry density decreases, the intrinsic water permeability increases accordingly, reflecting the dependence of permeability on the material’s compaction state.

Figure 3b shows a 3D illustration of effective water permeability ($k_{kozeny} k_{rl}$) – degree of saturation (S_l) and porosity (ϕ) path. The test data was available for two level of porosities : 0.33 (red colour) and 0.44 (blue colour). The effective water permeability increases following Eq. (7) and it reaches its maximum when full saturation is achieved, as all pores are filled with water, providing the maximum possible flow surface. The line in Fig. 3b represents a continuous calibration trend illustrating progressive saturation and porosity increase and is intended as a conceptual representation of a swelling pressure test. The final state of effective water permeability under saturated conditions is influenced by the initial porosity and the specific test conditions (swelling or compression) applied during the experiment.

The interpretation of oedometer tests (Romero et al. 2023) indicates that k_{effI} of the S/B mixture is approximately one order of magnitude lower than previously estimated. Therefore, a set of sensitivity analyses on effective water permeability is recommended for HM-G modelling of the GAST experiment to account for this variability and improve model accuracy. The calibrated parameters for the porosity-dependent permeability function of the S/B mixture are listed in Table 1. Laboratory test results (Manca 2015) indicate that the effective water permeability variation with degree of saturation is density dependent in the S/B mixture material. Since, the water is mainly stored in the bentonite, the compaction of the mixture causes a reduction of the bentonite void ratio. The anisotropy ratio of 10, representing the upper bound of the expected range and not assumed as a constant value within the model domain, was selected based on back-calculations performed to reproduce the permeability variations observed in the piezometer measurements. This

ratio was not treated as uniform across the domain, as the compaction layers exhibit varying characteristics (Fig. 1c). While previous studies (Sakaki et al. 2023; Lanyon et al. (2022) reported anisotropy ratios typically ranging from 3 to 5 or higher, the adopted value of 10 provided the best agreement with the experimental observations in certain sections of the model, considering the available material dataset and the underlying theoretical framework. Further refinement of this ratio can be carried out once the test data become publicly available. The observed anisotropy is attributed to the dynamic compaction process, which induces preferential particle alignment, leading to higher horizontal permeability relative to the vertical direction.

Gas Flow Mechanism and Gas Transport Model Parameters

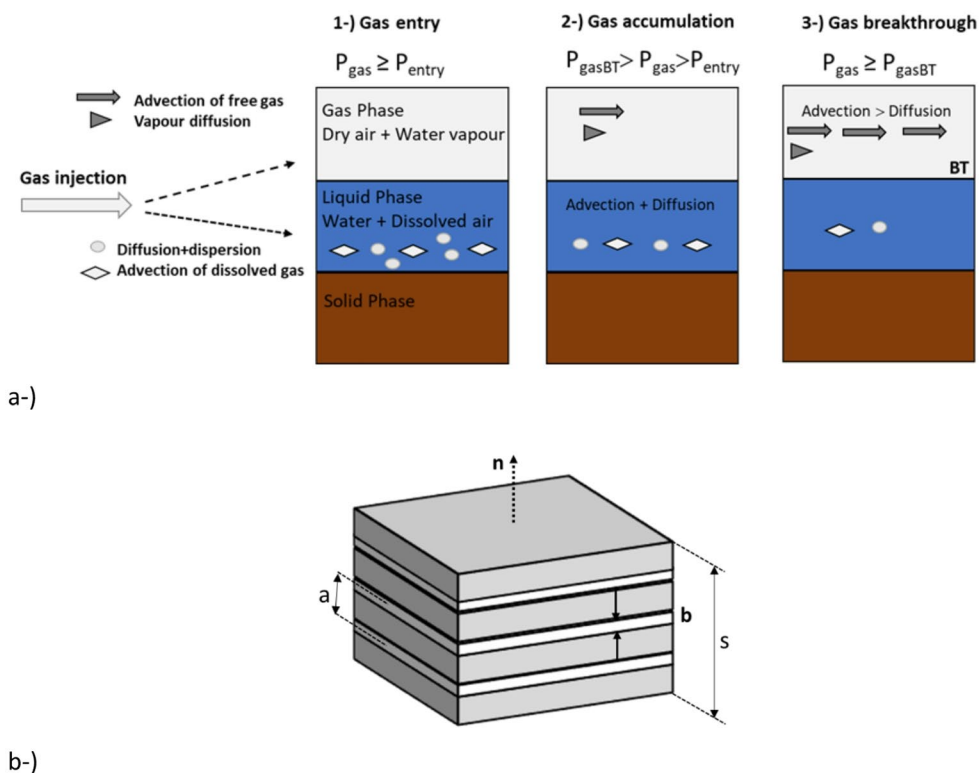
Gas transport into clay barriers is accompanied by the development of preferential gas flow pathways propagating through the clay (Horseman et al. 1999). Gas flow through clay based materials is mostly restricted to these pathways (Cuss et al. 2012; Harrington et al. 2019). Following to gas pressure reduction, these pathways may close under continuous stress conditions (Gonzalez-Blanco and Romero 2022; Gutiérrez-Rodrigo et al. 2015, 2021). In the case of increasing pressure, the previously closed pathways can be re-opened at a lower pressure than initially needed.

The multi-phase THM-G formulation used in CODE_BRIGHT considers three phases: gas, liquid and solid phase. The liquid phase consists of water and dissolved air while the gas phase is a mixture of dry air and water vapor. Figure 4a shows the corresponding phases and the fluxes under different gas pressure conditions (Toprak et al. 2025a). Gas accumulates in the system till reaching gas breakthrough pressure (BT). The moment when gas crosses the saturated material is referred to as “breakthrough.” The pressure required to achieve this breakthrough is termed the breakthrough pressure (P_{gasBT}). Below a threshold known as the gas entry pressure, gas transport occurs primarily through diffusion within the porewater (Condition 1). Once the gas entry pressure is exceeded, advection of free gas is initiated (Condition 2). Following gas breakthrough, gas advection becomes the dominant transport mechanism (Condition 3).

Diffusion of dissolved air and water vapour starts following the Condition 2 as shown in Fig. 4a. Diffusive (or non-advective) mass fluxes are usually described by Fick’s law (τ : tortuosity, ϕ : porosity, ρ_a : density of the phase gas, S_a : degree of saturation of the phase and D: diffusion coefficient, α : air or water vapor phase, ω_a^i :mass fraction of species i in phase α) :

$$i_a^i = - (\tau \phi \rho_a S_a D_a^i) \nabla \omega_a^i \tag{8}$$

Fig. 4 Gas fluxes under specific hydro-mechanical conditions (a) and 3D representation of strain-dependent permeability parameters (b)



Since the porosity is a parameter influencing diffusion, the distribution of diffusive fluxes is expected to be heterogeneous due to the variability in initial porosity observed in the GAST experiment.

Diffusion coefficient is temperature dependent:

$$\tilde{D}^i(T) = \frac{D(273.15 + T)^n}{p_g} \tag{9}$$

In the GAST simulation temperature is not constant and has a small influence in diffusion coefficient.

The mass of water vapour per unit volume of the gas phase ($\theta_g^w = \omega_g^w \rho_g$) is related to soil suction ($P_g - P_l$) and controlled by the psychrometric law:

$$\rho_g^w = (\rho_g^w)^0 \exp\left(-\frac{(P_g - P_l) M_w}{R(T + 273.15) \rho_l}\right) \tag{10}$$

where $(\rho_g^w)^0$ is the temperature-dependent vapour density at null suction (i.e. in contact with a planar surface). T is the temperature (C), M_w is the molecular mass of water (18.016 g/mol) and R is the universal gas constant (8.3143 J·mol/K). In other words, the psychrometric law expresses the balance of air relative humidity with the suction of the liquid water phase in the pores of the solid matrix.

The concentration of air dissolved in the liquid phase ($\theta_l^a = \omega_l^a \rho_l$) is linearly related to the partial pressure of air (P_a) in the gaseous phase through Henry's law:

$$\rho_l^i = \frac{\rho_l p_i M_i}{H M_w} \tag{11}$$

where M_a is the molecular mass of air, M_w the molecular mass of water and H is the Henry's constant (10000 MPa).

The effective permeability (Eqs. (7) and (17), k (m²), as defined by Brown 2002 is a key parameter in advective flow. In the advective flow expression (Eq. (12), μ (Pa.s) denotes the dynamic viscosity, P is pressure (Pa), ρ_a (kg/m³) is the density of the respective phase and g (m/s²) is the gravitational constant. During Condition 2, advection of dissolved gas occurs, where “ α ” represents gas dissolved into liquid phase. In contrast, under Condition 3, “ α ” denotes the gas in free state.

$$\mathbf{q}_\alpha = -\frac{k_{eff} \alpha}{\mu_\alpha} (\nabla P_\alpha - \rho_\alpha g) \tag{12}$$

The strain-dependent cubic-law formulation (Eqs. (13),(14) and (15)) adopted in this study follows the continuum implementation proposed by Olivella and Alonso 2008. In this approach, embedded fractures are not explicitly represented as discrete geometric entities within the mesh. Instead, their hydraulic influence is accounted for through an additional permeability contribution (Eq. (13) derived from the cubic law (Eq. (14) and combined with the matrix permeability (Eq. (5) at the element level. The governing two-phase gas–water transport equations remain those of a Darcy-based continuum formulation (Eq. (12), and the

cubic-law term modifies only the intrinsic permeability tensor. Accordingly, the present model does not simulate discrete fracture nucleation or propagation; rather, it represents strain-induced permeability enhancement within selected zones of the continuum domain, consistent with the methodology established in Olivella and Alonso 2008.

Laboratory tests indicate preferential gas flow behaviour in sand–bentonite mixtures during gas injection under GAST-like boundary conditions (Romero et al. 2023). In the present study, this behaviour is represented through permeability-enhanced zones embedded within a heterogeneous porous matrix. These predefined zones occupy a limited volumetric fraction of the three-dimensional model domain and reflect process-driven heterogeneity associated with compaction and gas injection, rather than explicit fracture network modelling. The formulation therefore provides a continuum-scale engineering representation of strain-induced permeability enhancement within a coupled THM-G framework. While explicit fracture-flow representations or multi-scale approaches may be adopted in future investigations where detailed fracture hydrodynamics are required, such developments fall beyond the scope of the present work.

In the present work, this strain-dependent permeability relationship provides a direct link between deformation and intrinsic gas permeability. For the numerical implementation, selected finite-element volumes within the 3D model domain are assigned cubic-law-based permeability behaviour to represent zones of potential permeability enhancement. Outside these zones, intrinsic permeability follows the porosity-dependent Kozeny-type formulation (Eq. (5)). In this study, a simplified representation is adopted in which the strain-dependent permeability function is independent of n and s .

The intrinsic gas permeability (k_g) is defined below, where k_{Kozeny} corresponds to the porosity-dependent permeability following the Eq. (5) and k_{Cubic} is shown in Eq. (14).

$$k_g = k_{Kozeny} + k_{Cubic} \tag{13}$$

As a part of strain-dependent permeability, k_{Cubic} depends on aperture characteristics where b_0 corresponds to initial aperture and b_{max} is the maximum aperture.

$$k_{Cubic} = \frac{b^3}{12a} \tag{14}$$

The aperture, “ b ” is variable and is influenced by the mean aperture distance (a) and the difference in strain ($\epsilon - \epsilon_0$) along the aperture’s normal direction (n).

$$b = b_0 + (\epsilon - \epsilon_0)a \leq b_{max} \tag{15}$$

The strain variable ϵ in Eq. (15) represents the normal strain component associated with dilatant deformation within the adopted continuum formulation. The strain range considered in the calibration (approximately 10^{-3} to 0.2) was selected through back-analysis to reproduce the intrinsic permeability evolution observed in laboratory gas injection tests. These strain values do not correspond to directly measured deformation but represent modelling parameters governing strain-induced permeability enhancement within the framework. The two parameter sets presented in Table 1 represent lower- and upper-bound configurations of strain-induced intrinsic permeability enhancement derived from experimental permeability observations. The first set corresponds to moderate dilation with limited permeability increase, whereas the second set represents enhanced dilation associated with pronounced permeability enhancement during gas advection. These parameter sets should therefore be interpreted as representative bounds for strain-induced permeability evolution within the continuum framework rather than as universal material constants or explicit geometric aperture properties.

A 3D illustration of porosity-deformation- k_{Cubic} path for two different porosity levels is presented in Fig. 5a. k_{Cubic} parameters are porosity independent, meaning that similar aperture characteristics can be observed across different porosity levels (Manca 2015). Consequently, the lines depicted in Fig. 5a are representative and were specifically prepared for the calibration process outlined in this study.

The relative gas permeability, k_{rg} , is defined as a function of gas saturation, where the gas saturation S_{eg} equals to $1 - S_l$; A is model parameter and Ω is power.

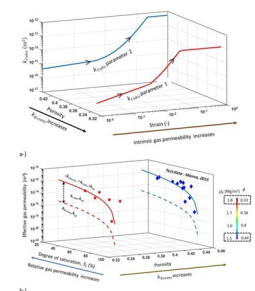
$$k_{rg} = AS_{eg}^\Omega \tag{16}$$

Finally effective gas permeability (k_{effg}) is a product of intrinsic and relative gas permeability:

$$k_{effg} = (k_{Kozeny} + k_{Cubic}) \tag{17}$$

Manca (2015) reported that the intrinsic gas permeability of S/B mixtures remained largely unaffected by variations in compaction density. However, gas breakthrough pressure

Fig. 5 Porosity-strain- k_{Cubic} path for two set of model parameters (a) and porosity-degree of saturation – effective gas permeability paths for two different compaction levels (b)



and the time required for breakthrough were influenced by compaction density. The calibration of the intrinsic and effective gas permeability model supports this experimental observation. The variation in k_{Kozeny} driven by porosity dependency is relatively minor compared to the variation observed in k_{Cubic} , which is strongly influenced by different aperture sizes and strain levels as illustrated in Fig. 5b. The intrinsic gas permeability is primarily governed by the strain-dependent permeability component (k_{Cubic}) rather than the porosity-dependent component (k_{Kozeny}). In this calibration, k_{Cubic} is observed to vary by up to two orders of magnitude (i.e., a factor of 100) depending on the strain level. In contrast, the variation in k_{Kozeny} resulting from changes in porosity is approximately fourfold.

Under the same degree of saturation, specimens compacted to two target dry densities (1.5 and 1.8 Mg/m³) exhibit different k_{Kozeny} values due to porosity-dependent permeability function (Eq. (5)). The porosity range of 0.3 to 0.44, shown in Fig. 5b corresponds to the variation in dry density observed in the field-scale GAST experiment according to Sakaki et al. (2023). Consequently, for the numerical modelling of GAST, at least two sets of k_{Cubic} parameters are recommended, based on observations from laboratory-scale gas permeability tests. In Fig. 5b, the porosity axis influences k_{Kozeny} but not k_{Cubic} . A significant reduction in effective gas permeability k_{effg} occurs upon wetting (Manca 2015), with effective gas permeability decreasing by several orders of magnitude when the degree of saturation exceeds 80%.

In this calibration process, the relative permeability parameters (Eq. (16)) were treated as spatially variable across the model domain. In the permeability-enhanced zones representing localised gas advection, the parameter A was calibrated to 100, reflecting the increase in gas permeability associated with advective gas flow. In contrast, in the remaining regions of the model (Fig. 9), where gas diffusion represents the primary transport mechanism, A was assigned a value of 20—an intermediate value consistent with the experimental observations reported by Romero et al. (2023).

Within the permeability-enhanced zones, the increase in intrinsic gas permeability resulting from strain is hydraulically coupled with the water retention behaviour. In these regions, the WRC becomes strain-dependent, reflecting the reduction in air-entry pressure associated with dilation. In the remaining parts of the model domain, hydraulic behaviour remains governed by the porosity-dependent WRC formulation.

To represent the reduction in air-entry pressure during the advection of free gas within dilatant regions of the model — here referred to as dilatant permeability-enhanced zones — a strain-dependent WRC (Olivella and Alonso 2008)

is required. In this case, the reference pressure for the air entry (P_ϵ) will depend on intrinsic permeability (Eq. (13)), therefore the k_{cubic} . Since k_{cubic} is strain-dependent, the air entry pressure correspondingly becomes a function of strain.

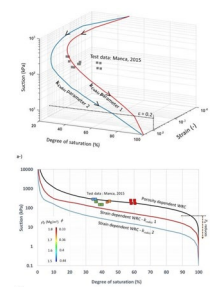
$$P_\epsilon = P_0 \frac{\sqrt[3]{(k_{Kozeny} + k_{Cubic})_0}}{\sqrt[3]{(k_{Kozeny} + k_{Cubic})}} \tag{18}$$

Using $P = P_\epsilon$ (Eq. (1)), the strain dependent WRC incorporating two set of k_{cubic} parameters is illustrated in Fig. 6a. As strain increases, intrinsic gas permeability rises, resulting in a corresponding reduction in air entry pressure.

In contrast to porosity-dependent WRC – where the reference pressure for the air entry (P_0) was calibrated as 100 kPa for a reference porosity (Fig. 2b) – the air entry pressure may decrease significantly under large strain levels, as shown in Fig. 6a. Strain-induced permeability enhancement within designated zones of the model leads to a local increase in intrinsic gas permeability, resulting in a reduction in gas entry pressure and a subsequent decline in the degree of saturation at constant capillary pressure.

Figure 6b presents a comparison between two representative strain-dependent water retention curves (WRC) — constructed using a mean strain value of 0.2 (selected as a representative case for permeability-enhanced zones within the model) — and a porosity-dependent WRC representative of the matrix behaviour. In Fig. 6b, the colours (red, orange, green, and blue) correspond to the experimental datasets, as indicated in the legend embedded within the figure. Different air-entry pressures were measured for different dry densities, as previously shown in Fig. 2a. To generate the strain-dependent WRC, k_{cubic} was first calculated for the given strain (Eq. (14)), followed by the computation of the corresponding P_ϵ using Eq. (18). This value of P_ϵ was then used to redraw the strain-dependent WRC, reflecting the influence of strain on water retention behavior. The results demonstrate a substantial reduction in P_0 from 100 kPa to 25 kPa and 7 kPa, depending on the parameterization applied to the strain-dependent WRC (for parameters see Table 1). Assuming the same shape parameter in Eq. (1),

Fig. 6 Strain dependent WRC curve for two set of parameters (a). Comparison of WRC according to dependency on porosity and strains. Reference strain used in this graph is 0.2 (b)



a reduction in P_0 leads to decrease in air entry pressure. The value of P_0 does not necessarily correspond directly to the air entry pressure. However, by maintaining the same magnitude of the shape parameter, reduced air entry pressures are achieved in strain-dependent WRC.

Mechanical Model Parameters

The calibration of mechanical model parameters requires the execution of at least one swelling pressure test and one oedometer test. To accommodate variations in mechanical modelling approaches, a swelling pressure test configuration was developed. Furthermore, the oedometer tests documented in Romero et al. (2023) were simulated. The configurations of the numerical models for both swelling pressure and oedometer tests are depicted in Fig. 7.

Two distinct mechanical models were evaluated to reproduce the swelling pressure evolution in an S/B mixture, with the objective of achieving a target reference swelling pressure of 200 kPa (Romero et al. 2023) for a specified dry density (1.6 Mg/m³). In the study conducted by Manca (2015), a swelling pressure of 130 kPa was reported for a dry density of 1.6 Mg/m³. BBM is one of the most widely used constitutive models for the simulation of the compacted bentonite in the design of final spent nuclear fuel repositories (Åkesson et al. 2010; Gens et al. 2009; Malmberg & Åkesson 2018; Sánchez et al. 2023 and Alcoverro et al. (2023), Toprak et al. 2017; and 2024). Barcelona Expansive Model (BExM) was developed by Alonso et al. (1999); Gens and Alonso (1992) and Sánchez et al. (2005) to better represent dual porosity in clay based materials.

The volumetric compressive behaviour of the BBM is defined by the elastic functions implemented for considering highly expansive soils. A brief description of BBM framework (Eq. (19) to (31)) is given below:

$$\text{Strain decomposition } d\epsilon_v = d\epsilon_v^e + d\epsilon_v^p \tag{19}$$

$$\text{Elastic volumetric strain } d\epsilon_v^e = \frac{\kappa_i(s)}{1+e} \frac{dp}{p} + \frac{\kappa_s(p,s)}{1+e} \frac{ds}{s+p_{at}} \tag{20}$$

$$\text{Load and Collapse (LC) yield locus } p - p_0(s, p_0^*) = 0 \tag{21}$$

$$\text{LC yield locus flow rule } d\epsilon_v^p = d\mu \tag{22}$$

$$\text{LC yield locus hardening rule } dp_0^* = \frac{1+e}{\lambda(0) - \kappa_{i0}} p_0^* d\epsilon_v^p \tag{23}$$

Plastic functions are described in BBM:

$$\lambda(s) = \lambda(0) ((1-r) \exp(-\beta s) + r) \tag{24}$$

Fig. 7 Oedometer test results (a) and its configuration (b). Swelling pressure vs. dry density (c) and $k_{k_{oedometry}}-s-p'$ path for BBM and BExM (d)

$$p_0(s, p_0^*) = p^c \left(\frac{p_0^*}{p^c} \right)^{\frac{\lambda(0) - \kappa_{i0}}{\lambda(s) - \kappa_{i0}}} \tag{25}$$

$$\text{Mean effective stress } p' = \frac{1}{3} (\sigma'_x + \sigma'_y + \sigma'_z) = p - \max(P_g, P_l) \tag{26}$$

$$\text{Plastic potential } G = q^2 - \alpha M^2 (p' + p_s) (p_0 - p') \tag{27}$$

The yield surface (F) depends on stresses and suction and can be expressed using stress invariants. Here, q represents the deviatoric stress, p denotes the mean total stress, α is the non-associativity parameter and M is the slope of the critical state line. When $\alpha = 1$, $F = G$ (associated plasticity). In this study, the associated plasticity was considered.

A recently implemented extension of BBM incorporates a direct correlation between swelling pressure (p_{swell}) and dry density (ρ_d). In this formulation (Eq. (28)), the parameter κ_s becomes suction dependent (Eq. (29)), with α_{ss} acting as a coupling term. The swelling pressure (p_{swell}) is computed as a function of dry density (Eq. (30) and Eq. (31)), where p_{ref} serves as an additional coupling term. $f_s(s)$ is suction component of the function and $f_p(p)$ is the pressure component of the function.

$$\kappa_s = \kappa_{s0} f_s(s) f_p(p) \tag{28}$$

$$f_s(s) = \exp(\alpha_{ss} s) \tag{29}$$

$$f_p(p) = 1 - \ln\left(\frac{p}{p_{ref}}\right) / \ln\left(\frac{p_{swell}(pd)}{p_{ref}}\right) \tag{30}$$

$$\log_{10}(1000 P_{swell}(d)) = c_0 + c_{1d} + c_{2d}^2 \tag{31}$$

An oedometer test conducted by Romero et al. (2023) on S/B mixture samples with a 50 mm diameter and an initial height of 10 mm was simulated (Fig. 7a and b). The initial water contents of the sample was 11.88% and the initial dry density was 1.7 Mg/m³. BBM was employed as the mechanical framework, with its calibrated parameters detailed in Table 2. The simulated results were compared against the experimental data obtained from laboratory tests (Fig. 7a), allowing for an assessment of the model's predictive capabilities. The numerical model (BBM) demonstrated a high predictive accuracy in capturing the variation of void ratio during loading and unloading. Additionally, the model effectively reproduced the expansion behavior upon soaking.

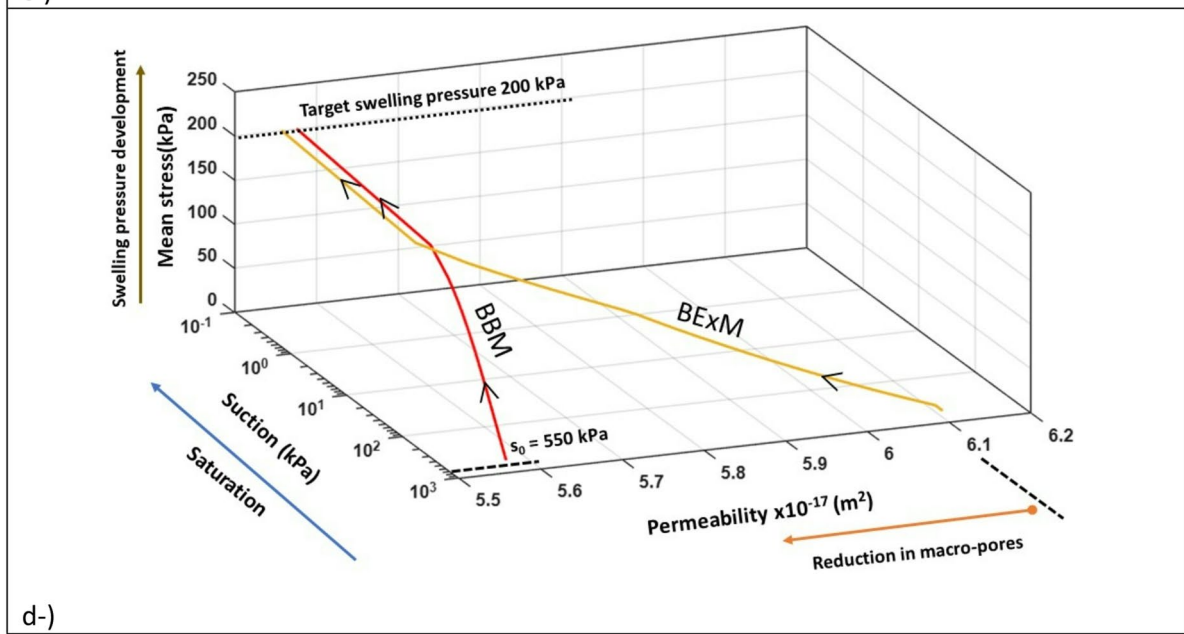
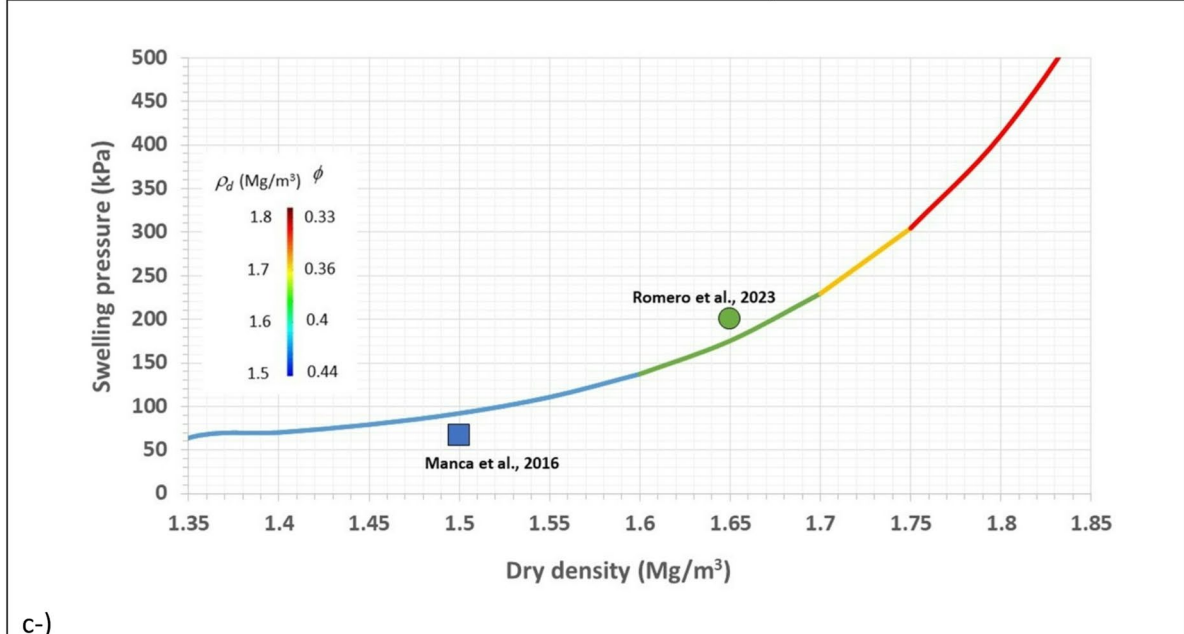
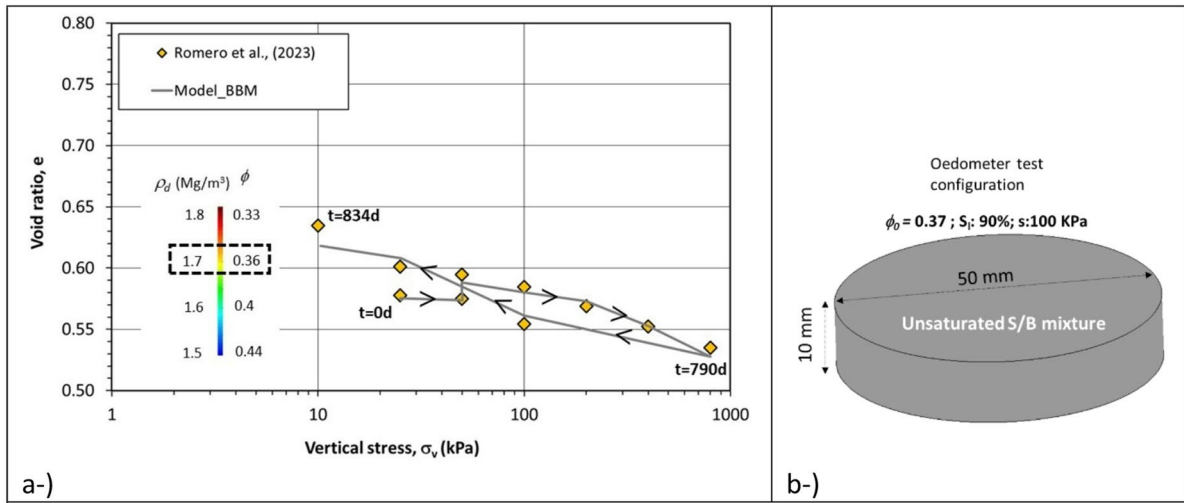


Table 2 Calibrated BBM parameters for S/B mixture targeting a swelling pressure of 200 kPa. Test data source : Romero et al. (2023)

Parameters	Units	Symbol	BBM
Parameters for elastic volumetric compressibility against mean net stress change	(-)	κ_i	0.017
Parameters for elastic volumetric compressibility against suction change	(-)	κ_s	0.015
Poisson ratio	(-)	ν	0.3
Coupling terms for the dry density dependent swelling pressure function	(-)	c_0	-3.85
	(-)	c_1	4.1e-3
	(-)	c_2	-3e-7
Reference pressure	MPa	p_{ref}	0.1
Slope of void ratio – mean net stress curve at zero suction	(-)	$\lambda(0)$	0.062
Parameters for the slope void ratio – mean net stress at variable suction	(-)	r	0.75
	(MPa ⁻¹)	b	0.3
Critical state line	(-)	M	1
Non-associativity parameter	(-)	a	1
Initial void ratio	(-)	e_0	0.66
Pre-consolidation mean stress for saturated soil	(MPa)	p_0^*	0.35

The swelling pressure–dry density relationship, calibrated using the extended BBM (Eq. 28 to Eq. (31)), is presented in Fig. 7c. The calibration was performed considering a target swelling pressure of 200 kPa (Romero et al. 2023) for an average dry density of 1.65 Mg/m³ and a corresponding pre-consolidation pressure of 300 kPa. The selected swelling pressure magnitude of 200 kPa for the average target dry density is consistent with the gas breakthrough pressure observed during laboratory experiment (Romero et al. 2023). It should be noted that the swelling pressure is influenced by initial conditions such as pre-consolidation pressure. At lower dry densities, for instance 1.4 Mg/m³, a swelling pressure of 67 kPa was reported (Manca et al. 2016). The presented curve is therefore indicative, representing a target swelling pressure for a given dry density under a specified pre-consolidation pressure. Final calibration of this relationship can be refined once experimental data from the GAST tests become publicly available.

The double structure model (BExM) incorporates two distinct porosity scales: micro-porosity and macro-porosity. In the model framework (from Eq. (32) to Eq. (40)), the microstructure is associated with clay particles and macrostructure corresponds to the macro-pores and coarse aggregates. The interaction between these two structural levels is significant, as microstructural behavior influences the response of the macrostructure.

Elastic volumetric strain of micro voids and macro voids:

$$d\epsilon_m^e = \frac{k_m}{1 + e_m} \frac{d(p' + s)}{(p' + s)} \tag{32}$$

$$d\epsilon_M^e = \frac{k_M}{1 + e_M} \frac{dp'}{p'} + \frac{k_s}{1 + e_M} \frac{ds}{s + p_{atm}} \tag{33}$$

Plastic strain of macro void :

$$d\epsilon_{vol}^{LC} + d\epsilon_{vol}^{SD} + d\epsilon_{vol}^{SI} = \frac{\lambda - \kappa}{(1 + e_M)} \frac{dp_0^*}{p_0^*} \tag{34}$$

Yield function :

$$F^{LC} = J^2 - \frac{M^2}{3} (p + p_t)(p_0 - p) \tag{35}$$

where p_t is the clay tensile strength, p_0 is the clay matrix isotropic yield locus and M is the slope of the critical state line in the $p - q$ diagram and J is the second invariant of the stress tensor. The following dependencies on suction are considered:

$$p_t = k_s s \tag{36}$$

$$p_0 = p^c \left(\frac{p_0^*}{p^c} \right)^{\frac{\lambda(0) - k_M}{\lambda(s) - k_M}} \tag{37}$$

$$\lambda(s) = \lambda(0) [(1 - r) \exp(-\beta s) + r] \tag{38}$$

$$F^{SD} = \gamma^{SD} - p - s \tag{39}$$

$$F^{SI} = p + s - \gamma^{SI} \tag{40}$$

The BExM model parameters are provided in Table 3. A subset of parameters related to micro-macro coupling functions was derived from Mokni (2016), while the remaining parameters were calibrated to achieve the target swelling pressure of 200 kPa. A comparative analysis of swelling pressure development under the BBM and BExM models is presented in Fig. 7e. In Eq. (5), ϕ represents the total porosity in BBM, whereas in BExM it corresponds to macro porosity “ ϕ_M ”. Since BBM considers total porosity, there is no reduction in intrinsic permeability during hydration at the evaluated location (central location). In contrast, in the BExM model, intrinsic permeability decreases during hydration due to the reduction of macro-pores. Ultimately, both models start from the same initial conditions and reach comparable magnitudes of swelling pressure and saturated water permeability; however, they exhibit distinct hydro-mechanical evolution paths. In particular, the development of stress under unsaturated conditions differs between the two formulations, reflecting their respective treatment of porosity and microstructural interactions.

Table 3 Barcelona Expansive Model (BExM) parameters. Test data source : Romero et al. (2023) and Mokni (2016)

Parameters	Units	Symbol	Value
Matrix elastic stiffness parameter at macro level for changes in mean stress	(-)	k_M	0.017
Matrix elastic stiffness parameter at micro level for changes in mean effective stress	(-)	k_m	0.015
Elastic macro stiffness parameter for changes in macro suction	(-)	k_s	0.01
Parameter micro-macro coupling functions when suction decrease (SD) is activated	(-)	f_{sdO}	-0.1
	(-)	f_{sd1}	1.1
	(-)	n_{sd}	2
Parameter micro-macro coupling functions when suction increase (SI) is active	(-)	f_{siO}	-0.1
	(-)	f_{sd1}	1.1
	(-)	n_{si}	0.5
Critical state line	(-)	M	1
Parameters for the slope void ratio – mean net stress at variable suction	(-)	r	0.75
	(MPa ⁻¹)	b	0.3
Reference pressure for the P_0 function	(MPa)	p^c	0.1
Slope of void ratio – mean net stress curve at zero suction	(-)	λ (0)	0.062
Pre-consolidation mean stress for saturated soil	(MPa)	p_0^*	0.35
Micro porosity	(-)	f_m	0.26
Macro porosity	(-)	f_M	0.14

Assessment of the Model Parameters

In this section, the performance and feasibility of the proposed hydro-mechanical and gas transport (HM-G) model parameters are evaluated. To this end, a numerical configuration was developed to reproduce an experimental sequence comprising an initial hydration stage followed by a gas injection phase, a procedure (Gutiérrez-Rodrigo et al. 2021) commonly employed in gas breakthrough tests on engineered barrier systems. Although this configuration does not correspond to a specific laboratory test, it is designed to represent the expected HM-G response of an S/B mixture, incorporating heterogeneity at a reduced scale.

The model configuration incorporates initial heterogeneity in porosity distribution—defined across four levels—to reflect variations induced by the dynamic compaction of the sand–bentonite mixture, consistent with observations from the GAST setup (Sakaki et al. 2023). Previous gas injection experiments have reported variations in aperture magnitudes across different clay-based materials (Wiseall et al. 2015; Gutiérrez-Rodrigo et al. 2021; Gonzalez-Blanco and Romero 2022). In the present model, these variations in aperture magnitude are not represented as explicit geometric fractures but are incorporated through predefined permeability-enhanced zones governed by the strain-dependent intrinsic permeability

relationship. Accordingly, for each of the four porosity levels, three permeability zones were established: two representing distinct levels of permeability enhancement associated with gas advection, and one corresponding to the intact matrix where diffusion-dominated transport prevails. The implementation of multiple permeability zones—typically including regions of permeability enhancement associated with localised gas advection and regions representing intact material—has been adopted in several repository-related modelling studies to simulate permeability evolution during gas injection tests. This approach has been applied to MX-80 bentonite in the context of the LASGIT experiment (Noghretab et al. 2024), to FEBEX bentonite in Spanish repository studies (Toprak et al. 2025a), and to Callovo–Oxfordian claystone (COx) in French in situ gas injection investigations (Rodríguez-Dono et al. 2024). These applications demonstrate that continuum-scale representations incorporating permeability-enhanced zones constitute an established methodology in the assessment of gas migration processes in clay-based nuclear waste repository systems.

Each porosity level occupies 25% of the total model volume, with the intact section accounting for 80% and the permeability-enhanced zones (connected and unconnected) for 20% of the respective subdomain (Fig. 8a). An initial suction of 0.55 MPa, consistent with the GAST setup, was adopted. The simulated domain measured 36 × 38 cm, representing a small-scale section. The hydration phase was simulated for 60 days, during which full saturation was achieved, followed by a 40-day gas injection phase with pressure increasing to 0.25 MPa. This was conducted under a short time scale to limit the contribution of gas diffusion and emphasize advective transport processes. Nitrogen gas was injected under isothermal conditions (20 °C). Boundary conditions were constrained to maintain constant-volume conditions throughout the simulation.

The material parameters used in the simulations were derived from this study (Hydro-gas: Table 1; Mechanical: Table 2). Figure 8 presents the resulting hydro-mechanical and gas transport responses. The distributions of porosity (Fig. 8b) and permeability (Fig. 8c) at the end of hydration stage (60 days) are closely aligned, reflecting the porosity-dependent permeability function. Under constant-volume conditions and given the small specimen size, variations in porosity during hydration were minimal. The permeability variation across the domain was approximately fourfold, corresponding closely to the imposed porosity distribution. Thus, the model reproduces, within the adopted framework, the expected dependence of permeability on porosity.

Figure 8d presents the distribution of the degree of saturation after 15 days of hydration, during which the modelled section has not yet reached full saturation. The lower part of the domain exhibits complete saturation, as it is located

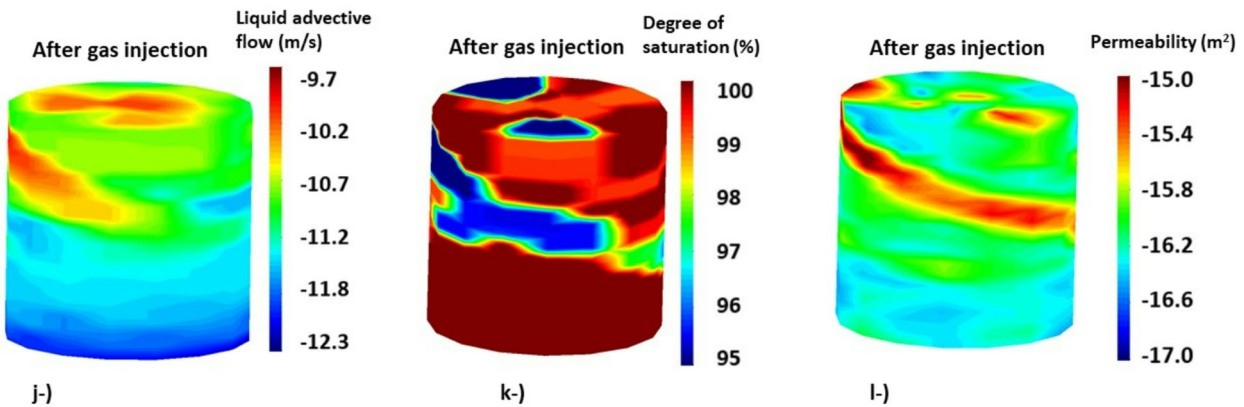
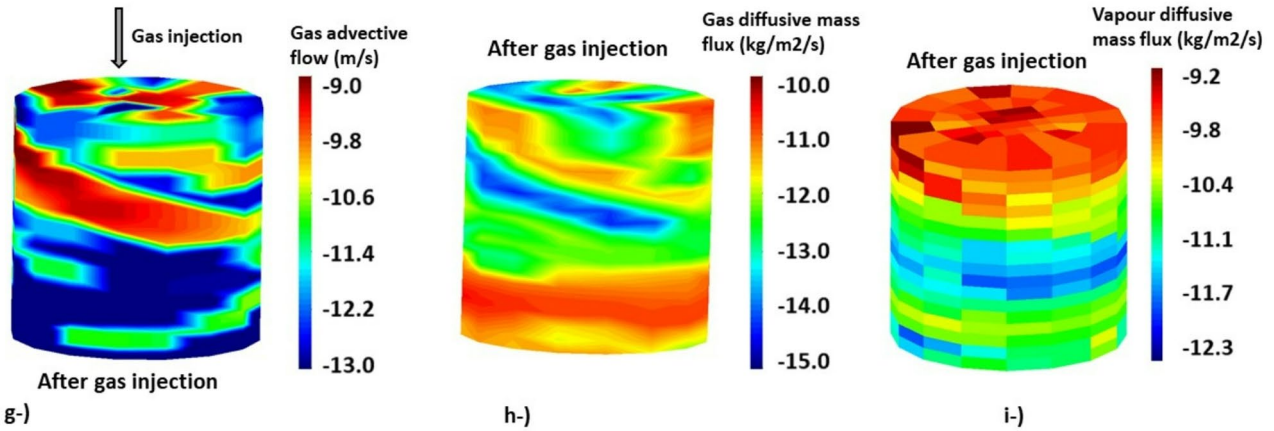
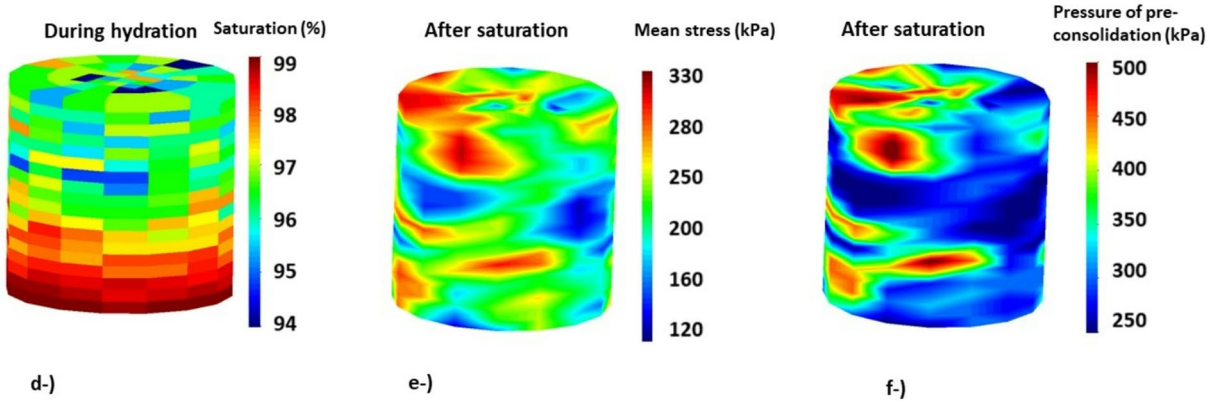
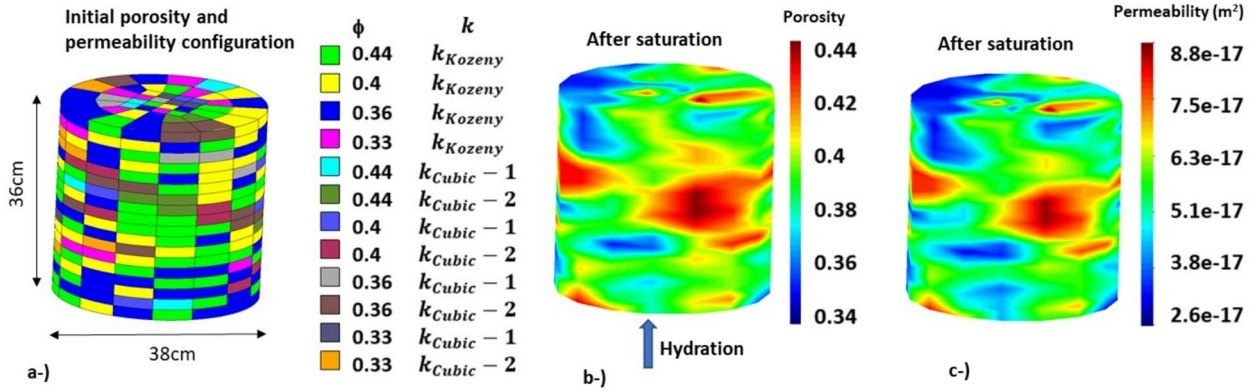


Fig. 8 Model configuration (a); distribution of porosity (b); permeability (c); degree of saturation (d); mean stress (e); pre-consolidation pressure (f); gas advective flow (g); gas diffusion (h); vapour diffusion (i); liquid advective flow (j); degree of saturation after gas injection (k); and permeability after gas injection (l)

closer to the hydration source. In contrast, the middle and upper regions remain partially unsaturated. Notably, certain zones in the upper part display lower saturation levels compared with intermediate sections, despite being further from the hydration boundary. This behaviour is attributed to the porosity-dependent nature of WRC and permeability parameters, which govern the local hydraulic response. Consequently, the observed heterogeneous distribution of the degree of saturation primarily arises from the spatial variability in porosity influencing the WRC.

The mechanical response—including the distribution of mean stresses and pre-consolidation pressures after hydration (at 60 days)—is presented in Fig. 8e and f, respectively. The simulation employed an extended Barcelona Basic Model (BBM) formulation to account for swelling pressure dependence on dry density (Fig. 7c). As expected, different porosity levels yielded distinct mean stress values, consistent with the corresponding pre-consolidation pressures.

Figure 8g illustrates the distribution of advective gas flow. As shown, gas advection is more pronounced in certain regions of the domain. The gas was injected from the upper boundary, and end-to-end advection of free gas was successfully achieved; however, the flow was localised within permeability-enhanced zones rather than occurring uniformly throughout the entire domain.

Figure 8h presents the distribution of non-advective fluxes, which include the diffusion of dissolved air and dispersion within the liquid phase. In contrast to advective gas flow, gas diffusion is active across the whole model domain, as the development of gas diffusion does not require the attainment of breakthrough pressure. Gas diffusion occurs even under very low gas injection pressures, although its magnitude is reduced in regions where advective gas flow is dominant. Vapour diffusion, shown in Fig. 8i, is also observed during gas injection, with the air phase defined as a mixture of air and water vapour. Since porosity is a controlling parameter for both dissolved air and vapour diffusion, the spatial distribution of vapour diffusion is heterogeneous. Higher diffusion values are observed near the top of the domain, corresponding to the injection boundary, while the remaining areas exhibit variable diffusion intensity reflecting the local heterogeneity of the system.

Another component of gas transport is the advection of dissolved gas within the liquid phase. Figure 8j presents the distribution of advective liquid flow at the end of the gas injection stage. The advective transport of dissolved gas was determined using Henry's law (Eq. (11)). The combined

effects of dissolved gas advection and diffusive fluxes are more pronounced before the attainment of gas breakthrough pressure. The magnitudes and temporal evolution of these processes have been recently calculated and discussed in detail in a recent publication (Toprak et al. 2025a), which reports results from a gas injection test performed on FEBEX material under a similar experimental configuration.

Finally, Fig. 8k and l presents the degree of saturation and permeability distribution (log scale) at the end of the gas injection stage. Unlike the hydration stage, the permeability pattern does not directly follow the porosity distribution (Fig. 8c), indicating the localisation of high-permeability zones associated with gas flow. The highest permeability values are concentrated within permeability-enhanced zones associated with localised gas advection, largely independent of the initial porosity levels. Desaturated zones are also observed in regions where advective flow is most pronounced (Fig. 8k). In other words, during the saturation phase, permeability is primarily governed by porosity, whereas during gas injection, it becomes controlled by the strain-induced permeability enhancement within designated zones rather than solely by the intrinsic porosity distribution.

It should be emphasised that although permeability-enhanced zones are assigned within the initial model configuration, the resulting gas flow behaviour cannot be inferred solely from the initial geometric distribution. During the hydration phase, coupled hydro-mechanical processes occur, including swelling, stress redistribution, porosity adjustment, and saturation changes, which modify intrinsic permeability prior to gas injection. Consequently, the permeability field at the onset of gas injection differs from the initial assignment. Furthermore, the strain-dependent permeability formulation allows intrinsic permeability to evolve locally during gas pressurisation. The resulting gas migration behaviour therefore reflects the coupled evolution of hydro-mechanical and transport processes rather than a direct consequence of the predefined spatial zoning.

To address potential realisation dependence associated with the assignment of permeability-enhanced zones within the heterogeneous model domain, we note that a detailed sensitivity analysis on alternative permeability zoning configurations was previously conducted in Toprak et al. 2025a. In that study, three-dimensional modelling of laboratory-scale gas injection tests on FEBEX material was performed using the same modelling framework and strain-dependent permeability formulation adopted in the present work. The analysis demonstrated that although the exact spatial localisation of permeability-enhanced regions may vary depending on their initial assignment, the global HM-G response—including breakthrough behaviour, permeability evolution, and overall advective flow characteristics—remains qualitatively consistent.

Overall, the simulation demonstrates the capability of the proposed model configuration to capture the coupled hydro-mechanical and gas transport processes while accounting for system heterogeneity. The model reproduces the evolution of porosity, degree of saturation, stress development, permeability, gas diffusion, and gas advection under GAST-like boundary conditions, comprising an initial saturation phase followed by gas injection.

The simulations presented here do not correspond to any GAST experimental data and should not be interpreted as part of the GAST experiment. However, they provide an indicative understanding of the THM-G behaviour of the S/B mixture at a small scale under heterogeneous conditions and a process sequence similar to that of the GAST experiment (saturation followed by gas injection).

In the small-scale representative model configuration presented in Sect. [Assessment of the Model Parameters](#), predefined permeability-enhanced zones provide a generic representation of potential gas migration regions within the continuum framework. In contrast, the full-scale GAST experiment includes multiple piezometers and total pressure cells distributed throughout the S/B mixture, enabling localisation of gas breakthrough and identification of dominant gas migration regions from measured pore pressure evolution. Consequently, in the actual GAST application, the spatial distribution of permeability-enhanced zones can be constrained and refined using experimental observations once the GAST data become publicly available.

Impact of Heterogeneity in a Representative Model Configuration for GAST

A representative model configuration (Fig. 9) was developed for the GAST experiment to incorporate process-driven heterogeneity and fully coupled HM-G behaviour.

The model accounts for spatial variations in dry density (porosity), air entry pressure, intrinsic and effective water and gas permeability, swelling pressure, and, consequently, gas breakthrough pressure.

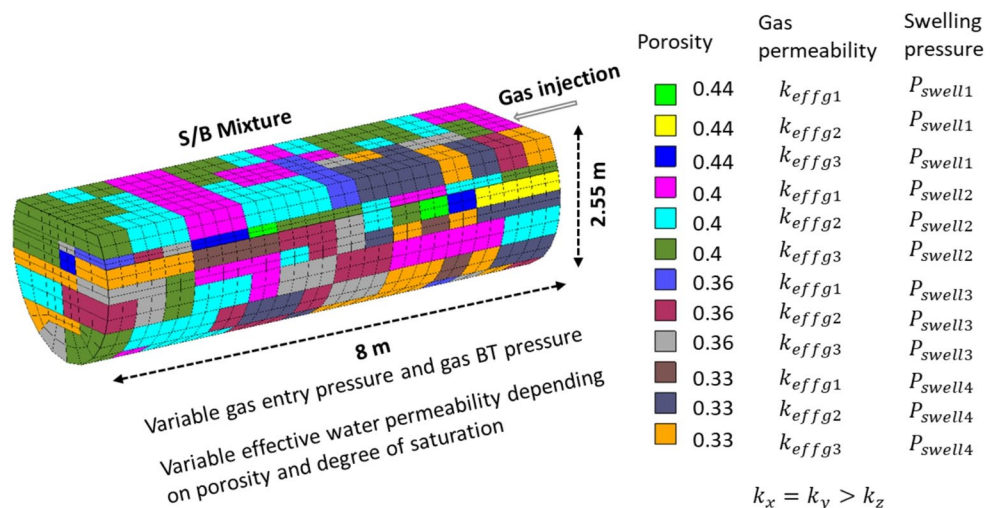
Simplified representations that do not incorporate heterogeneity and full-scale HM-G coupling can be useful for certain modelling objectives or preliminary analyses; however, they may not fully represent the complex behavior observed in the actual system. The non-uniform distributions of total pressure, liquid pressure, and gas pressure observed in the GAST experiment (Lanyon et al. 2022) cannot be accurately reproduced using a simplified model configuration (homogenous and not coupled). Therefore, as discussed in the methodology sub-section (Sect. [Introduction](#)), a ‘3D full modelling’ approach—characterized by heterogeneity, full coupling, and the inclusion of all stages prior to gas injection—is developed to achieve a realistic model configuration.

This configuration (Fig. 9) is valid when selecting BBM as the mechanical model. However, if the double structure model (BExM) is assigned as the mechanical model, an additional heterogeneity arises due to macro and micro-porosity variations.

The porosity field was divided into four zones (Fig. 1c). As discussed in Sect. [Assessment of the Model Parameters](#), for each porosity zone, at least three effective gas permeability sub-zones are required: two representing distinct levels of strain-induced permeability enhancement associated with gas advection, and one corresponding to the intact matrix where diffusion-dominated transport prevails. Consequently, the representative model configuration illustrated in Fig. 9 comprises a total of 12 zones, accounting for heterogeneity in both porosity and effective gas permeability.

In this representative configuration, effective gas permeability zones were assigned using a random spatial

Fig. 9 A representative model configuration illustrating initial porosity distribution and the zonation of model parameters



distribution owing to the absence of publicly available experimental localisation data. Their spatial definition can be refined and explicitly incorporated into the model geometry once the GAST test results become available.

During the hydration stages, the WRC follows a porosity-dependent formulation, as no gas-induced dilation is activated under fully saturated conditions. Upon gas injection in the experiment, changes in stress and saturation may lead to local permeability enhancement. In the numerical model, this behaviour is represented through a strain-dependent intrinsic permeability within predefined permeability-enhanced zones. Accordingly, once gas injection is initiated in the simulation, the WRC transitions to the strain-dependent formulation given by Eq. (18), reflecting the coupling between intrinsic permeability and air-entry pressure. As intrinsic permeability increases locally due to strain accumulation, the reference air-entry pressure decreases (Fig. 6b), facilitating gas accumulation within these regions of enhanced permeability in the S/B mixture.

The gas breakthrough (BT) pressure is significantly influenced by the swelling behavior of the aggregates. Variations in dry density, induced by dynamic compaction, lead to differences in pre-consolidation pressure (p_0^*), which in turn result in variable swelling pressures. Consequently, the swelling pressure variation must be considered not only for hydro-mechanical (HM) coupling but also for hydro-mechanical-gas (HM-G) processes.

Simultaneously, gas breakthrough pressure varies across different porosity zones, resulting in spatially heterogeneous gas migration behaviour. This response reflects the influence of heterogeneity in intrinsic permeability and breakthrough pressure, leading to localised gas advection within designated permeability-enhanced regions of the model.

The porosity zones depicted in Fig. 9 represent the initial conditions of the S/B mixture. However, due to hydration stages preceding the final gas injection, different sections of the S/B mixture will experience swelling or compression, leading to porosity variations. Consequently, gas breakthrough pressures will be determined by the final dry density prior to gas injection, rather than the initial dry density. Therefore, the hydration stages preceding the final gas injection must be modelled to accurately reproduce the overall response of the test.

A summary of the influence of system heterogeneity on the modelling design of GAST is provided in Table 4. The simulation of swelling behavior in the S/B mixture during hydration requires the application of an appropriate mechanical model, likely either double structure model (BExM) or BBM extended to account for dry density dependency of swelling pressure. This modelling should be conducted

within a complete 3D model domain to adequately capture the effects of process-driven heterogeneity. In other words, a 3D half-geometry may not adequately reflect the spatial variability of the system.

Although the models developed in this study incorporate calibrated HM-G parameters based on back-calculations and modelling of laboratory-scale tests, the cubic law for fluid permeability parameters discussed in (Sect. [Gas Flow Mechanism and Gas Transport Model Parameters](#)) are test-specific. In future gas injection experiments involving S/B mixtures, the orientation and magnitude of micro-apertures observed experimentally may vary. Consequently, the parameters of the cubic-law-based intrinsic permeability formulation should be recalibrated through test-specific back-analysis. As experimental data from ongoing or future tests are not yet publicly available, the present model adopts an assumed spatial distribution of effective gas permeability to represent heterogeneity within the continuum framework.

In Sect. [Assessment of the Model Parameters](#), a 3D model configuration of a small-scale sand–bentonite (S/B) mixture under GAST-like conditions was presented, and the overall THM-G response was discussed. The feasibility and performance of the model parameters were demonstrated in Fig. 8. In this section, the small-scale configuration is upscaled to represent conditions closer to those of the GAST experiment.

One of the key differences is that changes in porosity within the small-scale configuration were limited by the constant-volume boundary conditions. In contrast, in the GAST setup, due to the larger volume of the S/B mixture and its interaction with the surrounding granular bentonite, the influence of porosity variations is expected to be more significant. Furthermore, the GAST experiment includes multiple hydration and gas injection stages, which collectively influence the overall response, whereas the small-scale configuration considered only a single hydration and gas injection cycle.

The zoning quantification was performed to establish a representative model configuration that captures the minimum level of heterogeneity required to reproduce the expected hydro-mechanical–gas (HM-G) behaviour. In principle, the configuration could include more than 12 zones; however, increasing the number of zones would substantially increase model complexity and the number of calibrated parameters, particularly through the introduction of additional permeability-enhanced zones governed by distinct cubic-law parameter sets. The configuration presented here therefore reflects the minimum zoning considered necessary within the adopted modelling framework, but it

Table 4 Summary of Impact of heterogeneity in the representative model configuration of GAST

Concept	Parameter	Remark
Thermal	Porosity and temperature dependent vapour diffusion	Temperature serves as an input parameter in both the diffusion coefficient ((Eq. (9)) and the psychrometric law (Eq. (10)). As temperature variation at the experimental site is limited, thermo-mechanical coupling remains weak, with only minor local variations in suction and stress.
Hydraulic	Porosity-dependent permeability	Water intrinsic permeability (Eq. (5)) is porosity-dependent (Fig. 3a), and the initial porosity varies across the model domain (Fig. 1c). Additionally, porosity is not constant throughout the experiment due to the influence of hydration stages. When employing the BExM (from Eq. (32) to (40)), permeability depends on macro-porosity and tends to decrease during hydration (Fig. 7c).
	Relative water permeability	Relative water permeability (Eq. (6)) depends on degree of water saturation. S/B mixture was initially unsaturated. The saturation was not homogenous due to porosity-dependent permeability function.
	Porosity-dependent WRC	A porosity dependent WRC (Eqs. (2) and (3)) is necessary to account for the initial heterogeneous distribution of dry density. The reference pressure for air entry (Fig. 2b) is variable and porosity dependent.
Mechanic	Swelling pressure	Dynamic compaction of S/B mixture leads to variations in swelling pressure magnitudes, resulting from differences in initial dry density (from Eq. (28) to (31)) and compaction-induced heterogeneity (Eq. (25)). During gas injection, mean stress decreases as a result of de-saturation, in accordance with Eq. (26).
Gas	Porosity-dependent permeability	One component of the intrinsic gas permeability (Eqs. (5) and (13)) is porosity dependent (Fig. 5a).
	Relative gas permeability	Relative gas permeability (Eq. (16)) depends on degree of gas saturation. During gas injection, desaturation is expected to occur in zones near the injection point, leading to spatial variations in relative gas permeability.
	Strain-dependent permeability	One component of the intrinsic gas permeability (Eq. (14)), is governed by the parameters controlling the strain-dependent intrinsic permeability formulation (Fig. 5a).
	Strain-dependent WRC	Air entry pressure is strain-dependent (Eq. (18)) during the advection of gas in free state. Since aperture magnitudes observed in gas injection experiments are not uniform (Fig. 6), at least two sets of k_{Cubic} parameters are required.
	Gas diffusion	Diffusive fluxes (Eq. (8)) are porosity dependent, with higher porosity zones exhibiting enhanced diffusion activity until gas breakthrough occurs.
	Gas breakthrough pressure	The magnitude of gas breakthrough (BT) pressure is linked to the swelling pressure. Variability in swelling pressure (from Eq. (28) to (31)), driven by initial conditions, leads to corresponding variations in gas breakthrough pressure.

does not represent a unique solution. Alternative approaches could, for example, assign initial porosity using a variogram-based spatial distribution. In such cases, however, the definition and calibration of permeability-enhanced zones within that heterogeneous field would become more challenging. Different modelling teams, using alternative numerical codes and assumptions, may adopt other strategies depending on their methodological capabilities and objectives. The configuration proposed in this study should therefore be interpreted as a structured and computationally efficient continuum-scale representation of process-driven heterogeneity for the GAST experiment, rather than the only possible modelling approach.

Conclusions

This study aimed to develop a framework and methodology for defining the HM-G properties of S/B mixture (80% sand and 20% bentonite) through back-calculations and simulations of laboratory-scale tests. In addition, it sought to configure a representative process-driven heterogeneity model structure for the GAST experiment, incorporating variations in intrinsic and effective water and gas permeability, air entry pressure, gas breakthrough pressure, swelling pressure, and porosity. This heterogeneous structure was implemented within three-dimensional continuum model domain to support future full-scale simulations.

Calibration through oedometer, gas permeability and water retention curve tests enabled consistent estimation of swelling pressure, permeability, and gas transport properties within the adopted modelling framework. The subsequent implementation of these parameters in a small-scale 3D configuration allowed for the evaluation of their performance under sequential hydration and gas injection stages representative of GAST conditions.

Key findings Dynamic compaction during the emplacement of the S/B mixture leads to heterogeneous dry density distribution, resulting in initial porosity variability. Since hydro-mechanical and gas transport properties are largely governed by dry density, this initial heterogeneity should be incorporated into continuum-scale HM-G modelling of GAST.

Laboratory gas injection tests indicate spatially localised gas flow behaviour in sand–bentonite mixtures. In the present study, this behaviour is represented through predefined permeability-enhanced zones within a continuum formulation. These zones capture strain-induced intrinsic permeability enhancement associated with gas injection.

The initial heterogeneous porosity distribution was integrated with representative effective gas permeability zones in the GAST configuration, taking into account anisotropy in intrinsic permeability. Varying levels of swelling pressure, strain- and/or porosity-dependent water retention curves (WRCs), as well as strain- and/or porosity-dependent intrinsic water and gas permeability functions were considered. This representative configuration is intended to serve as a key component of the three-dimensional continuum modelling strategy proposed for GAST simulations.

Material model calibration Material properties—including a WRC dependent on porosity and strain, an effective water permeability dependent on porosity and degree of saturation, and an intrinsic gas permeability dependent on strain—were calibrated through experimental simulations and inverse modelling. Furthermore, mechanical model parameters accounting for double-structure interactions (i.e., micro- and macro-porosity) were calibrated accordingly. This study evaluates the capabilities and limitations of the adopted coupled formulations in representing the HM-G behaviour of the S/B mixture within the defined modelling scope.

Gas-S/B mixture interactions The configuration developed in this study considers that gas flow behavior in S/B mixtures is sensitive to the specific conditions of the investigated system. Interactions between gas and the S/B mixture under repository-relevant conditions can be represented within a calibrated continuum-scale numerical framework.

Future Applications The process-driven heterogeneity configuration developed in this study serves as a foundational basis for full-scale HM-G modelling of the GAST experiment. Once the experimental data become available, the assumed distribution of intrinsic gas permeability zones can be refined and localized using measured responses. Similarly, further calibration of liquid and gas permeability, as well as mechanical model parameters, can be performed to enhance the model's engineering-scale applicability. The proposed methodology provides a structured continuum-scale framework applicable to other field-scale investigations within the context of HM-G design for nuclear waste repositories, where accounting for process-driven heterogeneity is critical to model accuracy within the stated modelling assumptions.

Appendix

Notation list

Equation	Parameter	Unit	Symbol	
Water retention curve	Degree of liquid and gas saturation	-	S_l, S_g	
	Gas pressure	MPa	P_g	
	Liquid pressure	MPa	P_l	
	Shape parameter	-	y	
	Porosity dependent shape parameter		$y(\phi)$	
	Reference pressure (measured P at certain temperature)	MPa	P_0	
	Porosity dependent reference pressure	MPa	$P_0(\phi)$	
	Strain dependent reference pressure	MPa	$P_0(e)$	
	Porosity	-	ϕ	
	Parameter in $P_0(\phi)$	-	C	
	Parameter in $\lambda(\phi)$		D	
	Permeability	Intrinsic permeability of gas	m^2	k_{int}
		Porosity dependent permeability	m^2	k_{Kozeny}
Relative permeability in phase α (l:liquid, g:gas)		-	k_{rl}, k_{rg}, k_{ra}	
Relative permeability constant		-	A	
Relative permeability power		-	Ω	
Effective permeability of gas and liquid phase		m^2	k_{effl}, k_{effg}	
Cubic law for fluid permeability	Strain dependent gas permeability	m^2	k_{Cubic}	
	Initial aperture	m	b_0	
	Spacing of the fractures	m	a	
	Reference strain to calculate aperture variations	-	e_0	
	Maximum aperture	m	b_{max}	
Fick's law	Non-advective mass flux of species in phase α (air or water vapour)	$kg\,s^{-1}m^{-2}$	i_a^i	
	Phase density	$kg\,m^{-3}$	ρ_α	
	Tortuosity coefficient	-	τ	
	Diffusion coefficient of the phase α	$m^2\,s^{-1}$	D_a^i	
	Mass fraction of species in phase α	-	ω_a^i	
	Longitudinal dispersivity	m	d_l	
	Transversal dispersivity	m	d_t	
	Hydrodynamic dispersion coefficient	$m^2\,s^{-1}$	D'_a	
Psychrometric law and Henry's law	Vapour density at null suction	$kg\,m^{-3}$	$(\rho_g^w)^0$	
	Temperature	$^\circ C$	T	
	Molecular mass of water	kg/mol	M_w	
	Universal gas constant	J·mol/K	R	
	Molecular mass of air	kg/mol	M_a	
	Henry's constant	Pa	H	
Darcy	Advective flux in phase α	ms^{-1}	q_a	
	Intrinsic permeability of the phase α	m^2	k	
	Dynamic viscosity	Pa s	μ_a	
	Gravitational constant	ms^{-2}	g	
Equation	Parameter	Unit	Symbol	

Notation list

Equation	Parameter	Unit	Symbol	
Mechanical model - BBM	Elastic and plastic volumetric deformation	-	$\varepsilon_v^e, \varepsilon_v^p$	
	Volumetric stiffness parameter under changes of mean stress	-	κ_i	
	Volumetric stiffness parameter under changes of suction	-	κ_s	
	Coupling parameter for κ_s	-	α_{ss}	
	Coupling parameter for κ_s	-	α_{sp}	
	Coupling parameter for κ_s	-	p_{ref}	
	Suction	MPa	s	
	Void ratio	-	e	
	Pre-consolidation stress for saturated conditions	MPa	p_0^*	
	Pre-consolidation stress	MPa	p_0	
	Mean effective stress	MPa	p^l	
	Mean net stress	MPa	p	
	Slope of void ratio – mean stress curve at zero suction	-	$\lambda(0)$	
	Effective stress	MPa	σ^l	
	Deviatoric stress	MPa	q	
	Non-associativity parameter	-	α	
	Tensile strength in saturated conditions	MPa	p_s	
	Critical state line parameter	-	M	
	Plastic potential	-	G	
	Parameter defining the maximum soil stiffness	-	r	
	Parameter controlling the rate of increase of the soil stiffness with suction	MPa ⁻¹	β	
	Suction component of α_{ss} in dry density dependent swelling pressure function	-	$f_s(s)$	
	Pressure component of α_{ss} in dry density dependent swelling pressure function	-	$f_p(p)$	
	Model parameters in dry density dependent swelling pressure function	-	c_0, c_1, c_2	
	Mechanical model - BExM (Double structure model)	Elastic strains of micro-voids	-	ε_m^e
		Elastic strains of macro-voids	-	ε_M^e
Parameter micro-macro coupling functions when SD (suction decrease) is activated.		-	f_{sdO}	
		-	n_{sd}	
Parameter micro-macro coupling functions when SI (suction increase) is activated.		-	f_{si}	
	-	n_{si}		

Acknowledgements Financial support has been granted by the National Cooperative for the Disposal of Radioactive Waste of Switzerland (Nagra) through a collaboration agreement with CIMNE (Spain). The authors thank Clara Alvarado, Thomas Spillmann, Emiliano Stopelli, Stefan Finsterle, Stratis Vomvoris and Alexandros Papafotiou for technical assistance and useful discussions. The authors acknowledge support from project PID2022-141429OBI00, funded by the Spanish Ministry of Science/Research Agency MCIN/AEI/10.13039/501100011033/FEDER EU and the Spanish Ministry of Universities.

Author contributions E.T wrote the main manuscript. All authors reviewed the manuscript.

Funding Open Access funding provided by CERCA through the CRUE-CSIC agreement with Springer Nature.

Data availability Some of data used are available from the corresponding author by request.

Declarations

Competing interests The authors declare no competing interests.

Open Access This article is licensed under a Creative Commons Attribution 4.0 International License, which permits use, sharing, adaptation, distribution and reproduction in any medium or format, as long as you give appropriate credit to the original author(s) and the source, provide a link to the Creative Commons licence, and indicate if changes were made. The images or other third party material in this article are included in the article's Creative Commons licence, unless indicated otherwise in a credit line to the material. If material is not included in the article's Creative Commons licence and your intended use is not permitted by statutory regulation or exceeds the permitted use, you will need to obtain permission directly from the copyright holder. To view a copy of this licence, visit <http://creativecommons.org/licenses/by/4.0/>.

References

- Åkesson M, Kristensson O, Boergesson L, Dueck A, Hernelind J (2010) *THM modelling of buffer, backfill and other system components Critical processes and scenarios* (1404–0344). http://www.skb.se/upload/publications/pdf/TR10-11_Part_1webb.pdf. http://inis.iaea.org/search/search.aspx?orig_q=RN:42011399
- Alcoverro J, Pintado X, Olivella S, Toprak E, Niskanen M (2023) Analysis of the extension of the elastic parameters for modelling highly expansive unsaturated soils with the Barcelona Basic Model. *Adv Mater Sci Eng* 2023:1196011. <https://doi.org/10.1155/2023/1196011>
- Alonso EE, Gens A, Josa A (1990) A constitutive model for partially saturated soils. *Géotechnique* 40(3):405–430. <https://doi.org/10.1680/geot.1990.40.3.405>
- Alonso EE, Vaunat J, Gens A (1999) Modelling the mechanical behaviour of expansive clays. *Eng Geol* 54(1):173–183. [https://doi.org/10.1016/S0013-7952\(99\)00079-4](https://doi.org/10.1016/S0013-7952(99)00079-4)
- Brown GO (2002) Henry darcy and the making of a law. *Water Resour Res* 38(7):11–11-11-12. <https://doi.org/10.1029/2001WR000727>
- Cuss R, Harrington J, Noy D (2012) Final report of FORGE WP4. 1.1: The stress-path permeameter experiment conducted on Callovo-Oxfordian Claystone. <https://nora.nerc.ac.uk/id/eprint/514344>
- Damians IP, Olivella S, Gens A (2020) Modelling gas flow in clay materials incorporating material heterogeneity and embedded fractures. *Int J Rock Mech Min Sci* 136:104524. <https://doi.org/10.1016/j.ijrmmms.2020.104524>
- Delahaye CH, Alonso EE (2002) Soil heterogeneity and preferential paths for gas migration. *Eng Geol* 64(2):251–271. [https://doi.org/10.1016/S0013-7952\(01\)00104-1](https://doi.org/10.1016/S0013-7952(01)00104-1)
- Diomidis N, Cloet V, Leupin OX, Marschall P, Poller A, Stein M (2016) *Production, consumption and transport of gases in deep geological repositories according to the Swiss disposal concept* (1015–2636). http://inis.iaea.org/search/search.aspx?orig_q=RN:49016095
- EURAD – D6.7 (2024) Gas transport mechanism <https://www.ejp-eurad.eu/publications/eurad-d67-gas-transport-mechanisms>
- Gens A, Alonso EE (1992) A framework for the behaviour of unsaturated expansive clays. *Can Geotech J* 29(6):1013–1032. <https://doi.org/10.1139/t92-120>
- Gens A, Sánchez M, Guimarães LDN, Alonso EE, Lloret A, Olivella S, Huertas F (2009) A full-scale in situ heating test for high-level nuclear waste disposal: observations, analysis and interpretation. *Géotechnique* 59(4):377–399. <https://doi.org/10.1680/geot.2009.59.4.377>
- Gerard P, Harrington J, Charlier R, Collin F (2014) Modelling of localised gas preferential pathways in claystone. *Int J Rock Mech Min Sci* 67:104–114. <https://doi.org/10.1016/j.ijrmmms.2014.01.009>
- Gonzalez-Blanco L, Romero E (2022) A multi-scale insight into gas transport in a deep Cenozoic clay. *Geotechnique* 1–18. <https://doi.org/10.1680/jgeot.21.00208>
- Guo G, Fall M (2018) Modelling of dilatancy-controlled gas flow in saturated bentonite with double porosity and double effective stress concepts. *Eng Geol* 243:253–271. <https://doi.org/10.1016/j.enggeo.2018.07.002>
- Gutiérrez-Rodrigo V, Villar María V, Martín Pedro L, Romero Francisco J, Barcala José M (2015) Gas-breakthrough pressure of FEBEX bentonite. *Geol Soc Lond Spec Publ* 415(1):47–57. <https://doi.org/10.1144/SP415.4>
- Gutiérrez-Rodrigo V, Martín PL, Villar MV (2021) Effect of interfaces on gas breakthrough pressure in compacted bentonite used as engineered barrier for radioactive waste disposal. *Process Saf Environ Prot* 149:244–257. <https://doi.org/10.1016/j.psep.2020.10.053>
- Harrington JF, Graham CC, Cuss RJ, Norris S (2019) Gas network development in compact bentonite: key controls on the stability of flow pathways. *Geofluids* 2019:3815095. <https://doi.org/10.1155/2019/3815095>
- Horseman ST, Harrington JF, Sellin P (1999) Gas migration in clay barriers. *Eng Geol* 54(1):139–149. [https://doi.org/10.1016/S0013-7952\(99\)00069-1](https://doi.org/10.1016/S0013-7952(99)00069-1)
- Jockwer N, Wieczorek K (2008) Gas migration in the Opalinus Clay as a function of the gas injection pressure, HG-C Project, Final Report <https://edocs.tib.eu/files/e01fb09/610669885.pdf>
- Komine H, Ogata N (1999) Experimental study on swelling characteristics of sand-bentonite mixture for nuclear waste disposal. *Soils Found* 39(2):83–97. <https://doi.org/10.1139/t02-115>
- Lanyon GW, Herbert AW, Reinicke A (2022) GAST Status Report. Nagra Arbeitsbericht. NAB 21–17. Agra, Switzerland
- Malmberg D, Åkesson M (2018) Modelling the interaction between engineered and natural barriers. SKB Report, P-17-03. <https://www.skb.se/publikation/2491402/P-17-03.pdf>
- Manca D (2015) Hydro-chemo-mechanical characterisation of sand/bentonite mixtures with a focus on the water and gas transport properties EPFL. https://infoscience.epfl.ch/record/213649/files/EPFL_TH6790.pdf
- Manca D, Ferrari A, Laloui L (2016) Fabric evolution and the related swelling behaviour of a sand/bentonite mixture upon hydro-chemo-mechanical loadings. *Géotechnique* 66(1):41–57. <https://doi.org/10.1680/jgeot.15.P.073>
- Marschall P, Horseman S, Gimmi T (2005) Characterisation of gas transport properties of the Opalinus Clay, a potential host rock formation for radioactive waste disposal. *Oil Gas Sci Technol* 60(1):121–139. <https://doi.org/10.2516/ogst.2005008>
- Mokni N (2016) Analysis of hydro-mechanical behaviour of compacted bentonite/sand mixture using a double structure formulation. *Environ Earth Sci* 75(14):1. <https://doi.org/10.1007/s12665-016-5872-2>
- Nagra (2008) Effects of post-disposal gas generation in a repository for low- and intermediate-level waste sited in the Opalinus Clay of Northern Switzerland. Nagra Technical Report NTB 08–07. http://nagra.ch/wp-content/uploads/2022/08/e_ntb08-007.pdf
- Noghretab BS, Damians IP, Olivella S, Gens A (2024) Coupled hydro-gas-mechanical 3D modeling of LASGIT experiment. *Geomech Energy Environ* 40:100623. <https://doi.org/10.1016/j.gete.2024.100623>
- Norris S (2015) EC forge project: updated consideration of gas generation and migration in the safety case. *Geol Soc Lond Special Publications* 415(1):241–258. <https://doi.org/10.1144/SP415.8>
- Olivella S, Alonso EE (2008) Gas flow through clay barriers. *Géotechnique* 58(3):157–176. <https://doi.org/10.1680/geot.2008.58.3.157>
- Olivella S, Vaunat J, A., R.-D (2023) Code_Bright 2023 user's guide. U P d Catalunya. https://deca.upc.edu/en/projects/code_bright/downloads/users_guide
- Radeisen E, Shao H, Hesser J, Kolditz O, Xu W, Wang W (2023) Simulation of dilatancy-controlled gas migration processes in saturated bentonite using a coupled multiphase flow and elastoplastic H2M model. *J Rock Mech Geotech Eng* 15(4):803–813. <https://doi.org/10.1016/j.jrmge.2022.05.011>
- Rodriguez-Dono A, Zhou Y, Olivella S, Gens A (2024) Modelling a gas injection experiment incorporating embedded fractures and heterogeneous material properties. *Geomech Energy Environ* 38:100552. <https://doi.org/10.1016/j.gete.2024.100552>
- Romero E, Alvarado C, Lloret A (2023) New challenges in experimental unsaturated soil mechanics. Experimental upscaling of an engineered gas-permeable seal. *E3S Web Conf* 382:05001. <https://doi.org/10.1051/e3sconf/202338205001>
- Rüedi J, Teodori S, Spillmann T, Reinhold M, Trick T, Keller M, Steiner P, Isler S, Gräfe K, Garcia-Sinerz JL, Palacios Jimenez B, Jacobs F, Eiholzer L, Maurer HR, Tisato N, Marelli S (2012) Gas-Permeable Seal Test at GTS: As-Built Report. Nagra Arbeitsbericht NAB 12–59. Nagra, Switzerland

- Sakaki T, Sakabayashi K, Kawamoto K, Spillmann T (2023) Compaction-induced variability in the 80/20 sand-bentonite mixture: spatial variation in dry density at different scales in the laboratory and large-scale gas seal test. *Appl Clay Sci* 246:107146. <https://doi.org/10.1016/j.clay.2023.107146>
- Sánchez M, Gens A, do Nascimento Guimarães L, Olivella S (2005) A double structure generalized plasticity model for expansive materials. *International journal for numerical and analytical methods in geomechanics* 29(8):751–787. <https://doi.org/10.1002/nag.434>
- Sánchez M, Pomaro B, Gens A (2023) Coupled THM analysis of a full-scale test for high-level nuclear waste and spent fuel disposal under actual repository conditions during 18 years of operation. *Geotech* 73(5):418–438. <https://doi.org/10.1680/jgeot.21.00106>
- Seiphoori A (2015) Thermo-hydro-mechanical characterisation and modelling of Wyoming granular bentonite. <https://nagra.ch/en/downloads/technical-report-ntb-15-05-2/>
- Senger R, Romero E, Marschall P (2018) Modeling of gas migration through low-permeability clay rock using information on pressure and deformation from fast air injection tests. *Transp Porous Media* 123(3):563–579. <https://doi.org/10.1007/s11242-017-0962-5>
- Spillmann T, Senger R, Lanyon GW, Giroud N, Marschall P (2015) Preliminary Analyses and Numerical Modeling of the Gas Permeable Seal Test (Gast) At The Grimsel Test Site, Switzerland. In *Proceedings of the TOUGH Symposium 2015* (pp. 346–354). https://tough.lbl.gov/assets/files/02/events/symposia/toughsymposium15/Proceedings_TOUGHSymposium2015.pdf
- Tamayo-Mas E, Harrington JF, Brüning T, Shao H, Dagher EE, Lee J, Olivella S (2021) Modelling advective gas flow in compact bentonite: lessons learnt from different numerical approaches. *Int J Rock Mech Min Sci* 139:104580. <https://doi.org/10.1016/j.ijrmm.2020.104580>
- Tamayo-Mas E, Harrington JF, Damians IP, Olivella S, Radeisen E, Rutqvist J, Wang Y (2024) Advective gas flow in bentonite: development and comparison of enhanced multi-phase numerical approaches. *Geomechanics for energy and the environment*. 37:100528. <https://doi.org/10.1016/j.gete.2023.100528>
- Toprak E, Olivella S, Pintado X (2017) Coupled THM modelling of engineered barriers for the final disposal of spent nuclear fuel isolation. *Geol Soc Lond Spec Publ* 443(1):235–251. <https://doi.org/10.1144/SP443.19>
- Toprak E, Olivella S, Pintado X (2020) Modelling engineered barriers for spent nuclear fuel repository using a double-structure model for pellets. *Environ Geotech* 7(1):72–94. <https://doi.org/10.1680/jenge.17.00086>
- Toprak E, Olivella S, Pintado X, Niskanen M (2024) 3D THM modelling of Finnish spent nuclear fuel repository. *Front Built Environ* 10:1465051. <https://doi.org/10.3389/fbuil.2024.1465051>
- Toprak E, Olivella S, Gutiérrez-Rodrigo V, Villar María V, Martín Pedro L (2025a) 3D Hydro-Mechanical and Gas Transport Modelling (HM-G) of cyclic gas breakthrough tests on FEBEX Material. *Environmental Geotechnics ENGE-2024-180*. <https://doi.org/10.1680/jenge.24.00180>
- Toprak E, Olivella S, Pintado X, Niskanen M, Hassan MM, Kristensson KS (2025b) O. 3D Thermo-hydro-mechanical (THM) modelling of Full-Scale-InSitu- System-Test (FISST). *Geological Society of London, Special Publications* <https://doi.org/10.1144/gslspecpub2025-19>
- van Genuchten MT (1980) A closed-form equation for predicting the hydraulic conductivity of unsaturated soils. *Soil Sci Soc Am J* 44(5):892–898. <https://doi.org/10.2136/sssaj1980.03615995004400050002x>
- Villar MV (2007) Water retention of two natural compacted bentonites. *Clays Clay Miner* 55(3):311–322. <https://doi.org/10.1346/CMN.2007.0550307>
- Wiseall AC, Cuss RJ, Graham CC, Harrington JF (2015) The visualization of flow paths in experimental studies of clay-rich materials. *Miner Mag* 79(6):1335–1342. <https://doi.org/10.1180/minmag.2015.079.06.09>

Publisher's note Springer Nature remains neutral with regard to jurisdictional claims in published maps and institutional affiliations.